A novel study on hybrid physics-data-driven reduced-order modeling for aerodynamic load inversion under structural field uncertainties

Yaru Liu [a], Lei Wang [b,*], Xuan Zhou [c] , Zeshang Li [b], Yuewu Wang [d]

[a] *Department of Mechanical and Aerospace Engineering, The Hong Kong University of Science and Technology, Hong Kong 999077, China*
[b] *National Key Laboratory of Strength and Structural-Integrity, Institute of Solid-Mechanics, Beihang University, Beijing 102206, China*
[c] *School of Aeronautic Science and Engineering, Beihang University, Beijing 102206, China*
[d] *Beijing Key Laboratory on Nonlinear Vibrations and Strength of Mechanical Structures, Department of Mechanics, Beijing University of Technology, Beijing 100124, China*

ARTICLE INFO

ABSTRACT

Aerodynamic loads are crucial for the structural safety of aerospace vehicles. However, direct measurement or high-fidelity simulation remains challenging. In service, structural parameters are influenced by multi-source uncertainties, often characterized by limited samples and spatial variability. To address this, this paper proposes a novel aerodynamic load inversion method considering structural field uncertainties, which reconstructs load boundaries from sparse measurements. First, reduced-order modeling (ROM) is employed to project high-dimensional aerodynamic loads into low-dimensional subspaces based on spatial distribution features, transforming the load inversion problem into the prediction of feature coefficients. A physics-data-driven neural network (PDNN) is developed to predict these coefficients, integrating a data-driven module capturing the response-coefficient mapping relationship with a physics-based module that enforces physical consistency. This hybrid design improves the performance under small-sample and high-noise conditions. To model structural field uncertainties, the interval Karhunen-Loève decomposition (IKLD) is adopted to convert uncertain field into a finite set of uncertain parameters. An adaptive Kriging surrogate model (AKSM) is then used for uncertainty propagation, yielding the interval estimation of aerodynamic loads. The effectiveness of the proposed method is validated through numerical and experimental examples, demonstrating its high accuracy, robustness, and practical applicability, even under sparse measurements, noise interference and field uncertainties.

1. Introduction

Accurate information of aerodynamic loads is critical for structural safety evaluation and control system design of aerospace vehicles [1,2]. In complex flight environments, these loads are spatially distributed and rapidly time-varying, making direct measurement challenging due to limitations in deploying surface force or pressure sensors. Although alternative sensing techniques (such as inertial measurement units) are available, they cannot directly measure aerodynamic parameters and often yield low-accuracy

---

estimations. To overcome this challenge, this study proposes an indirect aerodynamic load inversion method that reconstructs the aerodynamic loads based on easily measurable structural responses, such as strain and acceleration.

This inversion process aims to map structural responses back to the corresponding loads, constituting a typical inverse problem in structural dynamics. Under the assumption of small deformations and negligible fluid-structure interactions, the aircraft can be modeled by linear elastic partial differential equations that provide physical constraints for load inversion. Numerous load inversion methods have been developed and can be broadly classified into frequency-domain and time-domain approaches [3–5]. In the frequency domain, He et al. [6] identified the power spectral density of random loads and found that inversion errors are amplified at low frequencies through convolution relationships between loads and responses. In time domain, inversion methods reconstruct load histories through convolution relationships between loads and responses. For instance, Pham et al. [7] employed the Duhamel integral, while Jiang et al. [8] adopted the Newmark method to establish load-response recurrence relations. More recently, Bayesian-based techniques, such as Kalman filtering, have gained popularity. Gillijns et al. [9,10] proposed a minimum-variance unbiased estimation algorithm that inverted loads using displacement and acceleration responses. Overall, time-domain methods dominate practical applications, as they can directly capture the time variations of short-duration and multi-type loads.

In general, the inversion of aerodynamic load faces two challenges of ill-posedness. First, aerodynamic loads are continuous in both space and time domains, while structural responses can only be measured at a limited number of sparse spatial locations. This makes it difficult to reconstruct continuous load distribution, necessitating the use of spatial dimensionality reduction techniques. For instance, Coates et al. [11] employed the Fourier series to approximate load distributions. Wu et al. [12,13] partitioned the load domain into subregions and used local interpolation functions within each region. Carpenter et al. [14] and Pham et al. [7] adopted proper orthogonal decomposition to represent surface pressure fields in low-dimensional subspaces. In these approaches, the distributed load inversion problem is transformed into the identification of basis coefficients, typically using least-squares minimization. The second challenge arises from the noise measurement in structural response data, which exacerbates the ill-posed nature of the inversion problem [15,16], causing small input errors to produce large deviations in the results. To improve robustness, regularization techniques are widely adopted. For example, Aucejo et al [17,18] proposed and experimentally validated several regularization strategies for noisy environments. More recent advances include sparse regularization and Bayesian regularization [19–21], which further enhance stability. It is worth noting, however, that the inversion results are highly sensitive to the choice of regularization parameters.

In recent years, data-driven methods have emerged as powerful alternatives to traditional physics-based load inversion methods. By leveraging machine learning algorithms, these methods learn the mapping between structural responses and aerodynamic loads from large historical datasets. For example, Cooper et al. [22] developed a neural network to predict the static loads on a wing rib via strain measurements. Chen et al. [23] used a multilayer perceptron (MLP) to estimate aerodynamic loads from surface pressure data, achieving high accuracy except near the boundaries of the training set. However, the performance of data-driven models is highly dependent on high-quality training data, which typically require expensive flight or wind tunnel experiments. Moreover, their generalization capability is typically limited, making them less reliable when applied to previously unseen conditions. Under such circumstances, physics-informed neural networks [24–26] have been proposed as a hybrid approach that incorporates governing physical laws and prior knowledge into the training process of data-driven models. They have shown potential in load inversion
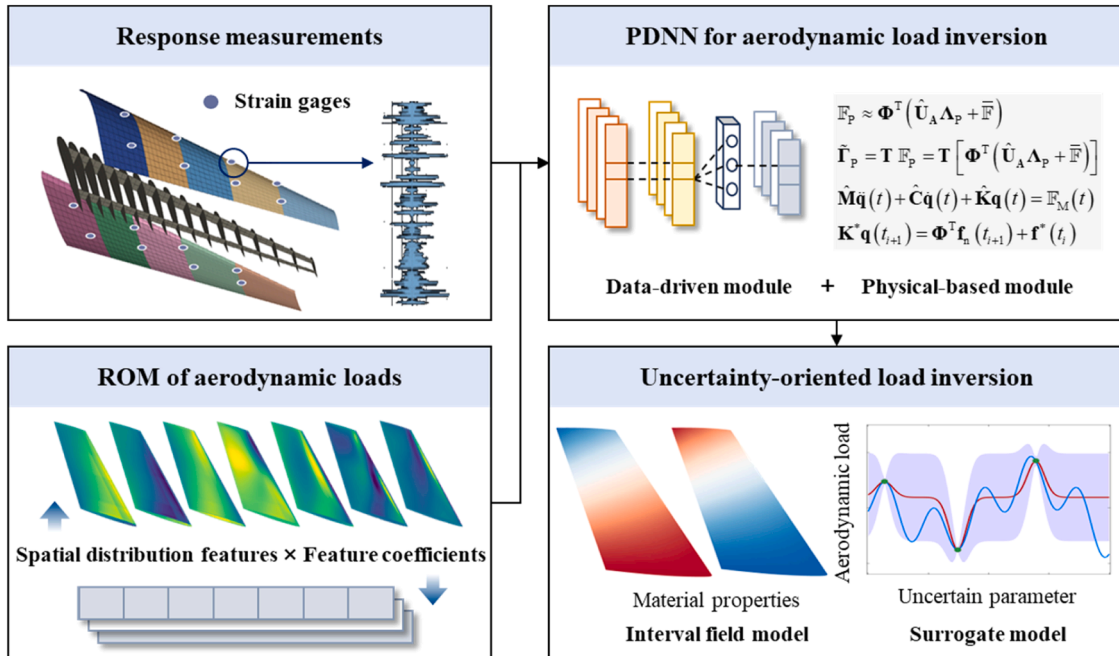

Fig 1. The logical framework of proposed method.

problems, particularly for concentrated loads such as impact and moving loads [27,28]. However, to the best of the authors' knowledge, their application to distributed aerodynamic load inversion remains unexplored.

Most existing aerodynamic load inversion methods are based on deterministic assumptions, treating structural parameters such as material properties and geometric dimensions as known and constant. However, in engineering applications, manufacturing and environmental fluctuations introduce uncertainties in these parameters [29–31], which may compromise the accuracy and stability of load inversion. Structural uncertainties can be categorized by their spatial characteristics into uncertain parameters and uncertain fields [32]. The former are represented by discrete variables, while the latter are modeled as spatially continuous functions with inherent correlations. In addition, the selection of uncertainty modeling approach depends on data availability: probabilistic models are suitable when sufficient samples exist for statistical inference [33,34], while non-probabilistic models are more preferable in data-scarce cases for boundary description [35]. Several uncertainty-oriented load inversion methods have been proposed that account for material dispersions, geometric deviations, and other modeling uncertainties, including our own work [36–38]. However, most of them have focus primarily on uncertain parameters. To more comprehensively characterize uncertainties, especially their spatial variation and correlation features, it is necessary to develop uncertainty quantification and propagation methods for uncertain fields.

In view of the above discussion, this study presents a hybrid physics-data-driven method for distributed aerodynamic load inversion under field uncertainties. A reduced-order modelling (ROM) is performed to reduce the spatial dimensionality of aerodynamic loads. A physics-data-driven neural network (PDNN) is developed to compute the feature coefficients, which can avoid the ill-posedness when measurement noises are involved. The interval field model is used to describe structural uncertainties with spatial variation and correlation. The remainder of this paper is outlined as follows. Section II introduces the fundamentals of response analysis under aerodynamic loads. Section III. details the inversion process using the ROM technique and PDNN model. Section IV. addresses uncertainty- oriented inversion with structural field uncertainties. Section V presents numerical and experimental validations of the proposed methodology. Finally, conclusions are given in Section VI. The overall schematic is illustrated in Fig. 1.

2. General statements of aerodynamic responses analysis

The essence of aerodynamic load inversion is reconstructing the spatiotemporal distribution of aerodynamic loads acting on aircraft structures from measured structural responses. This inverse problem is established on the corresponding forward problem of aerodynamic response analysis, which involves computational fluid dynamics (CFD) simulations, computational structural dynamics (CSD) simulations, fluid-structure interaction, mesh deformation and data mapping. In this study, the aircraft structure is assumed sufficiently rigid, allowing only the influence of fluid dynamics on structural dynamics to be neglected. Under this case, aerodynamic response analysis is reduced to three primary steps: CFD simulation CSD simulation, and aerodynamic load mapping. This section will introduce CFD and CSD simulations in detail.

2.1. Governing equation of compactional fluid dynamics (CFD)

Fluid dynamics is governed by the fundamental conservation laws of mass, momentum, and energy. Within the continuum hypothesis, the Navier-Stokes equations for different variables can be expressed in a unified form [39], i.e.,

$$\frac{\partial \mathbf{U}_F}{\partial t} + \nabla \cdot \mathbf{F}(\mathbf{U}_F) = \nabla \cdot \mathbf{G}(\mathbf{U}_F) + \mathbf{S} \tag{1}$$

where $\mathbf{U}_F = [\rho_F, \ \rho_F u, \ \rho_F v, \ \rho_F w, \ \rho_F E]^T$ represents the conserved variable vector; ρ_F denotes the fluid density; u, v and w indicate the velocity components in x, y and z directions; E means the total energy; $\mathbf{F}(\mathbf{U}_F)$ refers to the convective flux; $\mathbf{G}(\mathbf{U}_F)$ reflects the viscous flux; and $\mathbf{S}$ stands for the source terms. However, analytical solutions of Eq. (1) through mathematical methods is typically intractable, making numerical approaches essential. In the framework of the finite volume method, the fluid domain is divided into some discrete control cells and the governing equation over each cell (Ωe) is integrated as

$$\int_{\Omega e} \frac{\partial \mathbf{U}_F}{\partial t} \, d\Omega + \int_{\Omega e} \nabla \cdot \mathbf{F}(\mathbf{U}_F) \, d\Omega = \int_{\Omega e} \nabla \cdot \mathbf{G}(\mathbf{U}_F) \, d\Omega + \int_{\Omega e} \mathbf{S} \, d\Omega \tag{2}$$

By applying Gauss's divergence theorem, the volume integrals are transformed into surface integrals over the boundary ($\partial \Omega e$) of each cell, i.e.,

$$\int_{\Omega e} \frac{\partial \mathbf{U}_F}{\partial t} \, d\Omega + \int_{\partial \Omega e} \mathbf{F}_n \, d\mathbf{A} = \int_{\partial \Omega e} \mathbf{G}_n \, d\mathbf{A} + \int_{\Omega e} \mathbf{S} \, d\Omega \tag{3}$$

where $\mathbf{F}_n = \mathbf{F}(\mathbf{U}_F) \cdot \hat{\mathbf{n}}$ and $\mathbf{G}_n = \mathbf{G}(\mathbf{U}_F) \cdot \hat{\mathbf{n}}$ are the normal components of the convective and viscous fluxes, respectively; and $\hat{\mathbf{n}}$ denotes the unit outward normal vector. Assuming the conserved variables are uniform and constant within each cell, Eq. (3) can be transformed into

$$\frac{\partial \mathbf{U}_{F, e}}{\partial t} V_e + \sum_f \left(\mathbf{F}_{nf} - \mathbf{G}_{nf} \right) \mathbf{A}_f = \mathbf{S}_e V_e \tag{4}$$

where $\mathbf{U}_{F, e}$ demoted the cell-centered conserved variable; V_e denotes the cell volume; $\mathbf{F}_{nf}$ and $\mathbf{G}_{nf}$ relate to the convective and viscous vectors on surface f; and $\mathbf{A}_f$ is the surface area vector.

CFD simulations aim to determine the pressure distribution on the surface given initial and boundary conditions. By iteratively solving Eq. (4) until convergence, high-fidelity numerical solutions can be obtained, which are typically performed thorough commercial or open-source CFD software. In practice, the aircraft surface is discretized into triangular or quadrilateral elements, and its aerodynamic load can be computed by numerically integrating the pressure over discretized elements

$$\mathbb{F}_{fi} = -p_i s_i \mathbf{n}_i, i = 1, 2, \cdots, N_f \tag{5}$$

where p_i, $\mathbf{n}_i$ and s_i represent the aerodynamic pressure, unit normal vector and surface area of the i-th element; N_f is the number of fluid elements. It is noted that Eqs. (1)-(5) are presented in their general conservation form to illustrate the CFD framework. In practical aerodynamic computations, these equations are solved using closed formulations for specific turbulence models, such as unsteady Reynolds-Averaged Navier–Stokes equations (URANS) [40], rather than resolving all scales via direct numerical simulation. This approach achieves a practical balance between computational efficiency and predictive accuracy, which is crucial for engineering-oriented aerodynamic load inversion.

3. Governing equation of compactional structural dynamics (CSD)

The governing equation for structural dynamics under distributed dynamic loads can be expressed as

$$\rho_s(\mathbf{\Theta}) \frac{\partial^2 \mathbf{w}(\mathbf{\Theta}, t)}{\partial t^2} + C\left[\mathbf{\Theta}, \frac{\partial \mathbf{w}(\mathbf{\Theta}, t)}{\partial t}\right] + K[\mathbf{\Theta}, \mathbf{w}(\mathbf{\Theta}, t)] = \mathbf{f}(\mathbf{\Theta}, t) \tag{6}$$

where $\mathbf{\Theta}$ is the position vector; $\mathbf{w}(*)$ is the vector-valued displacement field of the structure; $\rho_s(*)$ means the material density distribution; $C(*)$ and $K(*)$ denote the damping and stiffness operators; and $\mathbf{f}(*)$ indicates the vector-valued external load distribution. Applying the finite element (FE) method to discretize this partial differential equation yields [36]

$$\mathbf{M}\ddot{\mathbf{u}}_s(t) + \mathbf{C}\dot{\mathbf{u}}_s(t) + \mathbf{K}\mathbf{u}_s(t) = \mathbb{F}_s(t) \tag{7}$$

where $\mathbf{M}$, $\mathbf{C}$ and $\mathbf{K}$ represent the $6N_s \times 6N_s$-dimensional global mass, damping and stiffness matrices, respectively (N_s is the number of FE nodes); $\mathbf{u}_s(t)$, $\dot{\mathbf{u}}_s(t)$ and $\ddot{\mathbf{u}}_s(t)$ denote the $6N_s \times 1$-dimensional global nodal displacement, velocity, and acceleration response vectors; $\mathbb{F}_s$ reflects the $6N_s \times 1$-dimensional nodal load vector derived from the CFD simulation results ($\mathbb{F}_f$). Due to the high computational cost from the large degrees of freedom (DOF) in aircraft structures, Eq. (7) is transformed into the modal coordinate system, i.e.,

$$\begin{cases} \widehat{\mathbf{M}}\ddot{\mathbf{q}}(t) + \widehat{\mathbf{C}}\dot{\mathbf{q}}(t) + \widehat{\mathbf{K}}\mathbf{q}(t) = \mathbf{\Phi}^T\mathbb{F}_s(t) = \mathbb{F}_M(t) \\ \mathbf{u}_s(t) = \mathbf{\Phi}q(t) \end{cases} \tag{8}$$

where $\mathbf{\Phi}$ is the $6N_s \times 6N_s$-dimensional modal matrix; $\widehat{\mathbf{M}} = \mathbf{\Phi}^T\mathbf{M}\mathbf{\Phi}$, $\widehat{\mathbf{C}} = \mathbf{\Phi}^T\mathbf{C}\mathbf{\Phi}$ and $\widehat{\mathbf{K}} = \mathbf{\Phi}^T\mathbf{K}\mathbf{\Phi}$ denote the $6N_s \times 6N_s$-dimensional diagonal modal mass, damping and stiffness matrices; $\mathbf{q}(t)$, $\dot{\mathbf{q}}(t)$ and $\ddot{\mathbf{q}}(t)$ are the $6N_s \times 1$-dimensional modal displacement, velocity and acceleration response vectors; and $\mathbb{F}_M(t) = \mathbf{\Phi}^T\mathbb{F}_s(t)$ is the modal load vector. This transformation decouples the system into independent single-DOF equations. To enhance efficiency, only the first M dominant modes are retained according to modal truncation criteria, leading to the reduced-order modal system, namely

$$\begin{cases} \widehat{\mathbf{M}}_M\ddot{\mathbf{q}}_M(t) + \widehat{\mathbf{C}}_M\dot{\mathbf{q}}_M(t) + \widehat{\mathbf{K}}_M\mathbf{q}_M(t) = \mathbf{\Phi}_M^T\mathbb{F}_s(t) \\ \mathbf{u}_s(t) \approx \mathbf{\Phi}_M\mathbf{q}_M(t) \end{cases} \tag{9}$$

where the subscript 'M' indicates reduced modal matrices and vectors.

The reduced system is solved using the Newmark method, a standard time integration scheme, which provides the following recursive relation

$$\mathbf{K}_M^*\mathbf{q}_M(t_{i+1}) = \mathbf{\Phi}_M^T\mathbb{F}_s(t_{i+1}) + \mathbf{f}^*(t_i) \tag{10}$$

where $\mathbf{K}^* = \frac{1}{\beta\Delta t^2}\widehat{\mathbf{M}}_M + \frac{\gamma}{\beta\Delta t}\widehat{\mathbf{C}}_M + \widehat{\mathbf{K}}_M$ and $\mathbf{f}^*(t_i) = \widehat{\mathbf{M}}_M\left[\frac{1}{\beta\Delta t^2}\mathbf{q}_M(t_i) + \frac{1}{\beta\Delta t}\dot{\mathbf{q}}_M(t_i) + \left(\frac{1}{2\beta}-1\right)\ddot{\mathbf{q}}_M(t_i)\right] + \widehat{\mathbf{C}}_M\left[\frac{\gamma}{\beta\Delta t}\mathbf{q}_M(t_i) + \left(\frac{\gamma}{\beta}-1\right)\dot{\mathbf{q}}_M(t_i) + \left(\frac{\gamma}{2\beta}-1\right)\ddot{\mathbf{q}}_M(t_i)\right]$

are the equivalent stiffness matrix and load vector; β and γ are algorithmic parameters. commonly $\beta = 0.25$ and $\gamma = 0.5$; and Δt denotes the time step. Combined with initial conditions $\mathbf{q}_M(t_0)$ and $\dot{\mathbf{q}}_M(t_0)$, the modal displacement, velocity and acceleration responses can be iteratively solved. Based on modal superposition theory, both global structural responses and localized structural responses at measurement points can be calculated. The responses corresponding to measurement points can be expressed as

$$\widehat{\mathbf{u}}_s(t) \approx \widehat{\mathbf{\Phi}}_M\mathbf{q}_M(t) \ , \ \widehat{\varepsilon}_s(t) \approx \widehat{\mathbf{\Psi}}_M\mathbf{q}_M(t) \ , \ \widehat{\ddot{\mathbf{u}}}_s(t) \approx \widehat{\mathbf{\Phi}}_M\ddot{\mathbf{q}}_M(t) \tag{11}$$

where $\widehat{\mathbf{u}}_s(t)$, $\widehat{\varepsilon}_s(t)$ and $\widehat{\ddot{\mathbf{u}}}_s(t)$ represent the localized displacement, strain and acceleration responses associated with the DOFs of measurement points; and $\widehat{\mathbf{\Psi}}$, $\widehat{\mathbf{\Phi}}$ are the observation modal matrix, obtained by selecting the corresponding rows from the reduced displacement and strain modal matrices that match the DOFs of the measurement points.

4. Aerodynamic load inversion via reduced-order modelling and physics-data-driven neural network (PDNN)

High-fidelity aerodynamic load distributions can be obtained from the CFD simulations described in Section II.A. However, this approach requires extensive iterations, making it computationally expensive and difficult to incorporate real-time flight measurements. This is limited under sudden or emergency conditions. In contrast, the CSD simulations introduced in Section II.B enable aerodynamic load reconstruction through inverse analysis of some measured responses (such displacements, strains and accelerations). Compared with conventional forward CFD simulations, this inverse method can significantly improve computational efficiency without substantially compromising accuracy.

5. Reduced-order modelling (ROM) for aerodynamic loads based on principal component analysis (PCA)

Aerodynamic loads are continuous in temporal and spatial dimensions. Reconstructing their spatial distributions from sparse measurements is inherently underdetermined, analogous to solving infinite variables with only finite equations. Even with the FE discretization, accurate nodal load reconstruction remains difficult because the number of unknowns still far exceeds the number of available equations. To address this, ROM is employed to project high-dimensional aerodynamic loads into low-dimensional subspaces while preserving the reconstruction fidelity to the original space. As a classical ROM technique, principal component analysis (PCA) can effectively extract the spatial distribution features (principal components) and their corresponding feature coefficients within reduced-order subspaces. This section focuses on the aerodynamic load inversion in structural domain, aiming to inverse the nodal load vector. To construct the reduced-order subspace, a representative aerodynamic load database is generated by parametric sampling of key flight parameters (e.g., Mach number and angle of attack), conducting CFD simulations for each sampled case, and mapping the aerodynamic loads from fluid to structural domain.

Aerodynamic response analysis requires a much finer fluid mesh than the structural mesh, resulting in non-conformal grids at the fluid–structure interface. Thus, the aerodynamic loads in the fluid domain must be mapped to the structural domain through interpolation methods. This mapping is governed by the principle of energy conservation, requiring the virtual work of fluid and structural loads on virtual displacements to be equal at the interface, namely

$$\delta W = \delta \mathbf{u}_f^T(t) \mathbb{F}_f(t) = \delta \mathbf{u}_s^T(t) \mathbb{F}_s(t) \tag{12}$$

where $\delta \mathbf{u}_f(t)$ and $\delta \mathbf{u}_s(t)$ represent the virtual displacements of the fluid and structural sides, related through the following kinematic transfer relationship

$$\delta \mathbf{u}_f(t) = \mathbf{H} \delta \mathbf{u}_s(t) \quad , \quad \mathbb{F}_s(t) = \mathbf{H}^T \mathbb{F}_f(t) \tag{13}$$

where $\mathbf{H}$ is the displacement mapping matrix. To construct this mapping, a global radial basis function (RBF) interpolation with thin plate splines (TPS) and polynomial basis functions [41] is used. The displacement vectors can be expressed as

$$\mathbf{u}_f(t) = \sum_{i=1}^{N_s} a_i(t) \phi_i(\mathbf{\Theta}_f) + \sum_{j=1}^{M} b_j(t) p_j(\mathbf{\Theta}_f) = \mathbf{\Phi}^T(\mathbf{\Theta}_f) \mathbf{a}(t) + \mathbf{p}^T(\mathbf{\Theta}_f) \mathbf{b}(t)$$

$$\mathbf{u}_s(t) = \sum_{i=1}^{N_s} a_i(t) \phi_i(\mathbf{\Theta}_s) + \sum_{j=1}^{M} b_j(t) p_j(\mathbf{\Theta}_s) = \mathbf{\Phi}^T(\mathbf{\Theta}_s) \mathbf{a}(t) + \mathbf{p}^T(\mathbf{\Theta}_s) \mathbf{b}(t) \tag{14}$$

where $\mathbf{\Theta}_f = \begin{bmatrix} \mathbf{x}_f, \mathbf{y}_f, \mathbf{z}_f \end{bmatrix} \in \mathbb{R}^{N_f \times 3}$ and $\mathbf{\Theta}_s = \begin{bmatrix} \mathbf{x}_s, \mathbf{y}_s, \mathbf{z}_s \end{bmatrix} \in \mathbb{R}^{N_s \times 3}$ are the spatial coordinates of fluid element centers and structural FE nodes; $\mathbf{x}_{f/s} = \begin{bmatrix} x_1, x_2, \cdots, x_{N_{f/s}} \end{bmatrix}^T, \mathbf{y}_{f/s} = \begin{bmatrix} y_1, y_2, \cdots, y_{N_{f/s}} \end{bmatrix}^T, \mathbf{z}_{f/s} = \begin{bmatrix} z_1, z_2, \cdots, z_{N_{f/s}} \end{bmatrix}^T$ are the three-directional Cartesian coordinate vectors; $\mathbf{\Phi}(\mathbf{\Theta}_{f/s}) = \begin{bmatrix} \phi_1(\mathbf{\Theta}_{f/s}), \phi_2(\mathbf{\Theta}_{f/s}), \cdots, \phi_{N_s}(\mathbf{\Theta}_{f/s}) \end{bmatrix}^T \in \mathbb{R}^{N_s \times N_{f/s}}$ represents the TPS basis functions centered at structural nodes, i.e., $\phi_i(\mathbf{\Theta}_{f/s}) = \| \mathbf{\Theta}_{f/s} - \mathbf{\Theta}_s^{(i)} \|^2 \ln \| \mathbf{\Theta}_{f/s} - \mathbf{\Theta}_s^{(i)} \| \in \mathbb{R}^{N_{f/s} \times 1}, i = 1, 2, \cdots, N_s; \mathbf{p}(\mathbf{\Theta}_{f/s}) = \begin{bmatrix} 1, \mathbf{x}_{f/s}, \mathbf{y}_{f/s}, \mathbf{z}_{f/s} \end{bmatrix}^T \in \mathbb{R}^{4 \times N_{f/s}}$ denotes monomial basis functions; and $\mathbf{a}(t) \in \mathbb{R}^{N_s \times 1}, \mathbf{b}(t) \in \mathbb{R}^{4 \times 1}$ are the interpolation coefficient vectors. However, RBF kernels alone are only conditionally positive definite, which may cause non-uniqueness in the interpolation coefficients [42]. To eliminate this null space, an additional constraint is imposed

$$\sum_{i=1}^{N_s} a_i(t) \mathbf{p}_{j,:}(\mathbf{\Theta}_s^{(i)}) = 0 \quad , \quad j = 1, 2, 3, 4 \quad \Rightarrow \quad \mathbf{p}(\mathbf{\Theta}_s) \mathbf{a}(t) = \mathbf{0} \tag{15}$$

which enforces the coefficient vector $\mathbf{a}(t)$ to be orthogonal to the polynomial space. This removes spurious degrees of freedom and guarantees uniqueness. With this constraint, the interpolation system is extended to

$$\begin{bmatrix} \mathbf{\Phi}^T(\mathbf{\Theta}_s) & \mathbf{p}^T(\mathbf{\Theta}_s) \\ \mathbf{p}(\mathbf{\Theta}_s) & \mathbf{0} \end{bmatrix} \begin{bmatrix} \mathbf{a}(t) \\ \mathbf{b}(t) \end{bmatrix} = \begin{bmatrix} \mathbf{u}_s(t) \\ \mathbf{0} \end{bmatrix} \quad , \quad \begin{bmatrix} \mathbf{\Phi}^T(\mathbf{\Theta}_f) & \mathbf{p}^T(\mathbf{\Theta}_f) \\ \mathbf{p}(\mathbf{\Theta}_s) & \mathbf{0} \end{bmatrix} \begin{bmatrix} \mathbf{a}(t) \\ \mathbf{b}(t) \end{bmatrix} = \begin{bmatrix} \mathbf{u}_f(t) \\ \mathbf{0} \end{bmatrix} \tag{16}$$

Eq. (16) is strictly nonsingular. Therefore, the coefficient vectors $\mathbf{a}(t)$ and $\mathbf{b}(t)$ are uniquely determined. Substituting Eq. (13) into Eq. (16), the displacement mapping matrix is derived as

$$\mathbf{H} = \begin{bmatrix} \mathbf{\Phi}^{\mathrm{T}}(\mathbf{x}_{\mathrm{f}}) & \mathbf{p}^{\mathrm{T}}(\mathbf{x}_{\mathrm{f}}) \end{bmatrix} \begin{bmatrix} \mathbf{\Phi}^{\mathrm{T}}(\mathbf{\Theta}_{\mathrm{s}}) & \mathbf{p}^{\mathrm{T}}(\mathbf{\Theta}_{\mathrm{s}}) \\ \mathbf{p}(\mathbf{\Theta}_{\mathrm{s}}) & \mathbf{0} \end{bmatrix}^{-1}_{[\,:\,,\,1:N_{\mathrm{s}}]} \tag{17}$$

where the subscript indicates the first N_{s} columns of the inverse matrix. Aerodynamic loads are consistently mapped from the fluid to the structural domain using Eqs. (13) and (17).

The load snapshots under different flight cases can be assembled into a matrix, i.e.,

$$\mathbb{F} = \begin{bmatrix} \mathbb{F}_{\mathrm{s}}^{(1)}(t_1)|_1 & \mathbb{F}_{\mathrm{s}}^{(1)}(t_2)|_1 & \cdots & \mathbb{F}_{\mathrm{s}}^{(1)}(t_{N_t})|_1 & \cdots & \mathbb{F}_{\mathrm{s}}^{(1)}(t_1)|_{N_P} & \mathbb{F}_{\mathrm{s}}^{(1)}(t_2)|_{N_P} & \cdots & \mathbb{F}_{\mathrm{s}}^{(1)}(t_{N_t})|_{N_P} \\ \mathbb{F}_{\mathrm{s}}^{(2)}(t_1)|_1 & \mathbb{F}_{\mathrm{s}}^{(2)}(t_2)|_1 & \cdots & \mathbb{F}_{\mathrm{s}}^{(2)}(t_{N_t})|_1 & \cdots & \mathbb{F}_{\mathrm{s}}^{(2)}(t_1)|_{N_P} & \mathbb{F}_{\mathrm{s}}^{(2)}(t_2)|_{N_P} & \cdots & \mathbb{F}_{\mathrm{s}}^{(2)}(t_{N_t})|_{N_P} \\ \vdots & \vdots & \ddots & \vdots & \ddots & \vdots & \vdots & \ddots & \vdots \\ \mathbb{F}_{\mathrm{s}}^{(N_s)}(t_1)|_1 & \mathbb{F}_{\mathrm{s}}^{(N_s)}(t_2)|_1 & \cdots & \mathbb{F}_{\mathrm{s}}^{(N_s)}(t_{N_t})|_1 & \cdots & \mathbb{F}_{\mathrm{s}}^{(N_s)}(t_1)|_{N_P} & \mathbb{F}_{\mathrm{s}}^{(N_s)}(t_2)|_{N_P} & \cdots & \mathbb{F}_{\mathrm{s}}^{(N_s)}(t_{N_t})|_{N_P} \end{bmatrix} \tag{18}$$

where $\mathbb{F} \in \mathbb{R}^{N_{\mathrm{s}} \times (N_t \times N_P)}$ represents the snapshot matrix; N_P denotes the number of parameter samples; and N_t is number of uniform temporal sampling points across all flight cases. Typically, it satisfies $N_{\mathrm{s}} \gg N_P \times N_t$. To address potential systematic biases of the snapshot matrix, mean-centering normalization is applied, namely

$$\mathbf{A} = \mathbb{F} - \overline{\mathbb{F}} \tag{19}$$

where $\overline{\mathbb{F}} \in \mathbb{R}^{N_{\mathrm{s}} \times 1}$ denotes the mean spatial distribution features, i.e. the average nodal load.

Perform singular value decomposition on the mean-centered snapshot matrix, namely

$$\mathbf{A} = \mathbf{U}_{\mathbf{A}} \mathbf{\Sigma}_{\mathbf{A}} \mathbf{V}_{\mathbf{A}}^{\mathrm{T}} = \sum_{i=1}^{r} \sigma_i \mathbf{U}_{\mathbf{A},\,[:,i]} \mathbf{V}_{\mathbf{A},\,[:,i]}^{\mathrm{T}} \tag{20}$$

where $\mathbf{U}_{\mathbf{A}} \in \mathbb{R}^{N_{\mathrm{s}} \times N_{\mathrm{s}}}$ and $\mathbf{V}_{\mathbf{A}} \in \mathbb{R}^{(N_t \times N_P) \times (N_t \times N_P)}$ are orthogonal matrices containing the left and right singular vectors (correspond to the eigenvectors of $\mathbf{A}\mathbf{A}^{\mathrm{T}}$ and $\mathbf{A}^{\mathrm{T}}\mathbf{A}$); $\mathbf{\Sigma}_{\mathbf{A}} = \mathrm{diag}\{\sigma_1, \sigma_2, \cdots, \sigma_r, 0, \cdots, 0\} \in \mathbb{R}^{N_{\mathrm{s}} \times (N_t \times N_P)}$ is a diagonal matrix of non-negative singular values sorted in descending order (obtained from square roots of eigenvalues of $\mathbf{A}\mathbf{A}^{\mathrm{T}}$ or $\mathbf{A}^{\mathrm{T}}\mathbf{A}$); σ_i represents the i-th singular value; $\mathbf{U}_{\mathbf{A},\,[:,i]}$ and $\mathbf{V}_{\mathbf{A},\,[:,i]}$ relate to the i-th columns of $\mathbf{U}_{\mathbf{A}}$ and $\mathbf{V}_{\mathbf{A}}$; and r denotes the matrix rank, typically satisfying $r = N_P \times N_t$ in the ROM of aerodynamic loads. Define $\mathbf{U}_{\mathbf{A}}$ as the projection matrix, whose columns are regarded as the orthogonal basis functions characterizing the spatial distribution features of the aerodynamic loads. Given $N_{\mathrm{s}} \gg N_P \times N_t$, direct computing $\mathbf{U}_{\mathbf{A}}$ is computationally expensive, and the following formulation can be employed to improve efficiency

$$\mathbf{U}_{\mathbf{A},\,[:,i]} = \frac{1}{\sigma_i} \mathbf{A} \mathbf{V}_{\mathbf{A},\,[:,i]} \tag{21}$$

Moreover, singular values indicate the energy contribution of the principal components. Typically, the first 10% (or even 1%) of singular values account for over 99% of the total energy [43], suggesting that appropriate truncation preserves accuracy. The truncation order (N_{b}) is determined using the cumulative variance contribution ratio, i.e.,

$$\Xi = \sum_{i=1}^{N_{\mathrm{b}}} \sigma_i^2 \Bigg/ \sum_{i=1}^{N_P \times N_t} \sigma_i^2 \geq \xi \tag{22}$$

where ξ is a predefined threshold. The truncated approximation is then given by

$$\mathbf{A} \approx \widehat{\mathbf{U}}_{\mathbf{A}} \widehat{\mathbf{\Sigma}}_{\mathbf{A}} \widehat{\mathbf{V}}_{\mathbf{A}}^{\mathrm{T}} = \sum_{i=1}^{N_{\mathrm{b}}} \sigma_i \mathbf{U}_{\mathbf{A},\,[:,i]} \mathbf{V}_{\mathbf{A},\,[:,i]}^{\mathrm{T}} = \widehat{\mathbf{U}}_{\mathbf{A}} \mathit{\Lambda} \tag{23}$$

where $\widehat{\mathbf{U}}_{\mathbf{A}} \in \mathbb{R}^{N_{\mathrm{s}} \times N_{\mathrm{b}}}$, $\widehat{\mathbf{V}}_{\mathbf{A}} \in \mathbb{R}^{(N_t \times N_P) \times N_{\mathrm{b}}}$ and $\widehat{\mathbf{\Sigma}}_{\mathbf{A}} = \mathrm{diag}\{\sigma_1, \sigma_2, \cdots, \sigma_{N_{\mathrm{b}}}\} \in \mathbb{R}^{N_{\mathrm{b}} \times N_{\mathrm{b}}}$ represent the first N_{b} components; and $\mathit{\Lambda} = \widehat{\mathbf{\Sigma}}_{\mathbf{A}} \widehat{\mathbf{V}}_{\mathbf{A}}^{\mathrm{T}} = \widehat{\mathbf{U}}_{\mathbf{A}}^{\mathrm{T}} \mathbf{A}$ denotes the feature coefficient matrix in the reduced-order subspace, specifically

$$\mathit{\Lambda} = \begin{bmatrix} \mathit{\Lambda}^{(1)}(t_1)|_1 & \mathit{\Lambda}^{(1)}(t_2)|_1 & \cdots & \mathit{\Lambda}^{(1)}(t_{N_t})|_1 & \cdots & \mathit{\Lambda}^{(1)}(t_1)|_{N_P} & \mathit{\Lambda}^{(1)}(t_2)|_{N_P} & \cdots & \mathit{\Lambda}^{(1)}(t_{N_t})|_{N_P} \\ \mathit{\Lambda}^{(2)}(t_1)|_1 & \mathit{\Lambda}^{(2)}(t_2)|_1 & \cdots & \mathit{\Lambda}^{(2)}(t_{N_t})|_1 & \cdots & \mathit{\Lambda}^{(2)}(t_1)|_{N_P} & \mathit{\Lambda}^{(2)}(t_2)|_{N_P} & \cdots & \mathit{\Lambda}^{(2)}(t_{N_t})|_{N_P} \\ \vdots & \vdots & \ddots & \vdots & \ddots & \vdots & \vdots & \ddots & \vdots \\ \mathit{\Lambda}^{(N_{\mathrm{b}})}(t_1)|_1 & \mathit{\Lambda}^{(N_{\mathrm{b}})}(t_2)|_1 & \cdots & \mathit{\Lambda}^{(N_{\mathrm{b}})}(t_{N_t})|_1 & \cdots & \mathit{\Lambda}^{(N_{\mathrm{b}})}(t_1)|_{N_P} & \mathit{\Lambda}^{(N_{\mathrm{b}})}(t_2)|_{N_P} & \cdots & \mathit{\Lambda}^{(N_{\mathrm{b}})}(t_{N_t})|_{N_P} \end{bmatrix} \tag{24}$$

In this ROM framework, the snapshot matrix of aerodynamic loads is approximated as the product of a small number of spatial distribution features and their corresponding feature coefficients. A new snapshot sample can be then projected into the low-dimensional subspace as

$$\mathit{\Lambda}_{\mathrm{New}}(t) = \widehat{\mathbf{U}}_{\mathbf{A}}^{\mathrm{T}} [\mathbb{F}_{\mathrm{s}}(\mathbf{P},\,t)|_{\mathrm{New}} - \overline{\mathbb{F}}] \tag{25}$$

where Λ_{New} is the feature coefficient vector for the new sample. Conversely, the original aerodynamic load distribution can be rapidly reconstructed from the low-dimensional feature coefficients by

$$\mathbb{F}_s(t)|_{\text{New}} \approx \widehat{\mathbf{U}}_{\mathbf{A}} \Lambda_{\text{New}}(t) + \overline{\mathbb{F}} \tag{26}$$

Therefore, the aerodynamic load inversion problem is reformulated as identifying the feature coefficients within a reduced-order subspace. This framework (illustrated in Fig. 2) significantly reduces both parameter dimensionality and computational cost, enabling efficient inversion of high-dimensional distributed loads from sparse measurements.

6. Feature coefficient inversion using sparse measurements via a PDNN framework

As outlined in the Introduction, feature coefficient inversion methods can be classified into physics-based and data-driven approaches. Physics-based methods project the structural governing equations into the modal space and reconstruct modal loads using inverse Newmark methods, following our previous work [36]. Feature coefficients are then computed via the least-squares methods based on the relationship between modal and physical loads

$$\Lambda(t) = \left[\left(\mathbf{\Phi}^{\mathrm{T}} \widehat{\mathbf{U}}_{\mathbf{A}} \right)^{\mathrm{T}} \left(\mathbf{\Phi}^{\mathrm{T}} \widehat{\mathbf{U}}_{\mathbf{A}} \right) \right]^{-1} \left(\mathbf{\Phi}^{\mathrm{T}} \widehat{\mathbf{U}}_{\mathbf{A}} \right)^{\mathrm{T}} \left[\mathbb{F}_{\mathrm{M}}(t) - \mathbf{\Phi}^{\mathrm{T}} \overline{\mathbb{F}} \right] \tag{27}$$

These methods offer clear physical interpretability but suffer from the ill-posed nature of inverse problems, being sensitive to measuring noise and initial conditions. Even small perturbations can lead to large inversion errors. Although regularization techniques can alleviate this issue, its performance strongly depends on the choice of parameters, which remains challenging.

In contrast, for data-driven methods, structural responses ($\mathbf{\Gamma}$) at measurement points under aerodynamic load snapshots are first obtained via CSD simulations (Section II.B), i.e.,

$$\mathbf{\Gamma} = \begin{bmatrix} \mathbf{\Gamma}^{(1)}(t_1)|_1 & \mathbf{\Gamma}^{(1)}(t_2)|_1 & \cdots & \mathbf{\Gamma}^{(1)}(t_{N_t})|_1 & \cdots & \mathbf{\Gamma}^{(1)}(t_1)|_{N_P} & \mathbf{\Gamma}^{(1)}(t_2)|_{N_P} & \cdots & \mathbf{\Gamma}^{(1)}(t_{N_t})|_{N_P} \\ \mathbf{\Gamma}^{(2)}(t_1)|_1 & \mathbf{\Gamma}^{(2)}(t_2)|_1 & \cdots & \mathbf{\Gamma}^{(2)}(t_{N_t})|_1 & \cdots & \mathbf{\Gamma}^{(2)}(t_1)|_{N_P} & \mathbf{\Gamma}^{(2)}(t_2)|_{N_P} & \cdots & \mathbf{\Gamma}^{(2)}(t_{N_t})|_{N_P} \\ \vdots & \vdots & \ddots & \vdots & \ddots & \vdots & \vdots & \ddots & \vdots \\ \mathbf{\Gamma}^{(N_m)}(t_1)|_1 & \mathbf{\Gamma}^{(N_m)}(t_2)|_1 & \cdots & \mathbf{\Gamma}^{(N_m)}(t_{N_t})|_1 & \cdots & \mathbf{\Gamma}^{(N_m)}(t_1)|_{N_P} & \mathbf{\Gamma}^{(N_m)}(t_2)|_{N_P} & \cdots & \mathbf{\Gamma}^{(N_m)}(t_{N_t})|_{N_P} \end{bmatrix} \tag{28}$$

where N_{m} represent the number of measurement points. These responses are regarded as network inputs, while the corresponding feature coefficients Λ obtained through the ROM framework in Section III.A, are regarded as network outputs. A neural network $NN(*)$ for feature coefficient inversion can be defined as

$$\Lambda = NN(\mathbf{\Gamma}) \tag{29}$$

Once trained, the network can directly process response measurements to estimate feature coefficients. By bypassing matrix inversion, data-driven methods avoid ill-posedness and show improved robustness to initial conditions. However, their effectiveness depends heavily on the quality of training data. Due to inevitable discrepancies between simulated and actual aerodynamic loads and responses, data-driven networks may capture spurious mappings inconsistent with physical laws, which increases the risk of over-fitting or underfitting, particularly under noise interference or with limited training data.

To combine the interpretability of physical-based methods with the robustness of data-driven methods, a PDNN model is proposed that embeds physical laws into the network architecture. As illustrated in Fig. 3, PDNN consists of two interconnected modules: the data-driven module and the physics-based module.

The data-driven module is designed to map the structural responses at measurement points to the feature coefficients of aerodynamic loads. According to the Newmark method, the response at a given time step depends not only on the concurrent load but also on responses from preceding time steps. This suggests that the aerodynamic load inversion should incorporate both current and subsequent structural responses. Conventional neural networks typically employ one-to-one input-output mappings, overlooking the
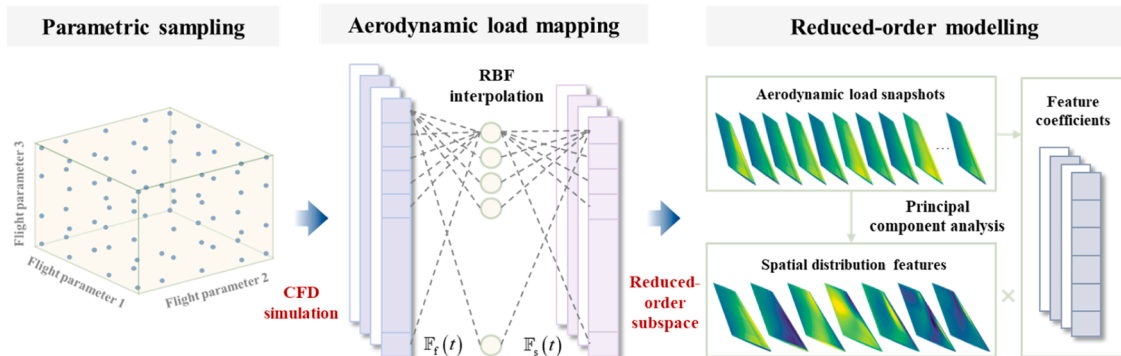

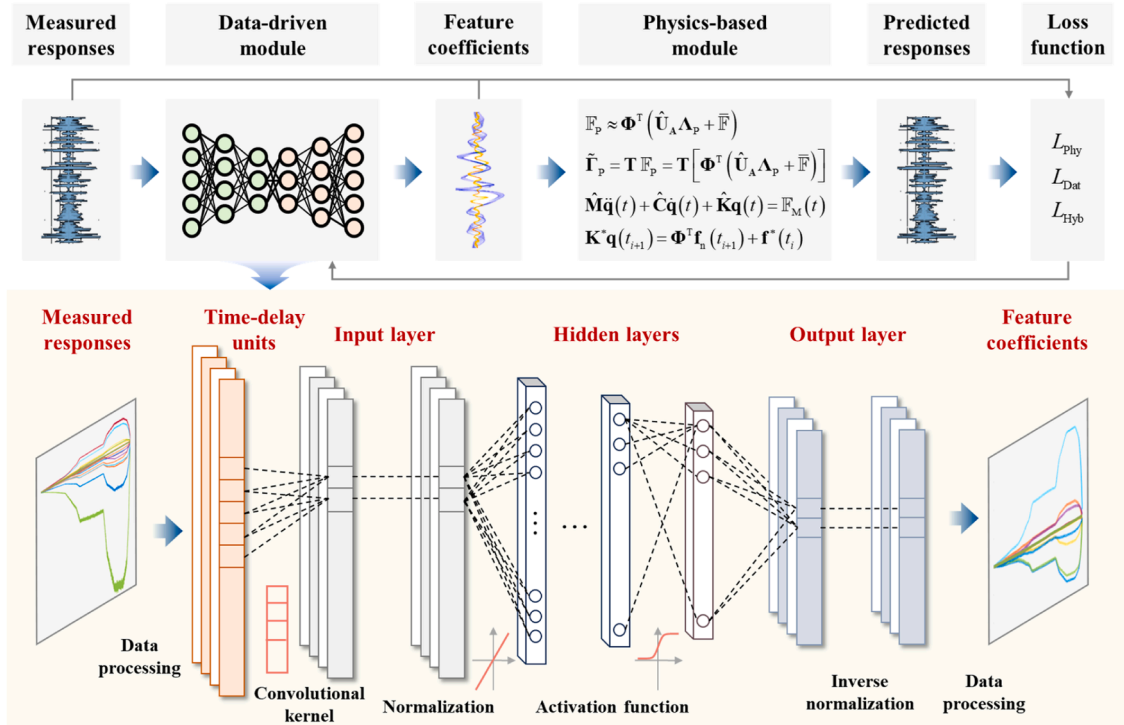**Fig 2.** Schematic of the ROM framework.

Fig 3. Schematic of the PDNN architecture.

inherent temporal dependencies in structural dynamics. To overcome this limitation, time-delay units are introduced before the input layer to capture dynamic characteristics of response sequences. A convolutional kernel is applied to perform weighted integration over the fixed-length time window, yielding a synthesized response ($\widetilde{\Gamma}$) as

$$\widetilde{\Gamma}(t_i)|_k = \sum_{j=1}^{D} \mathrm{E}_j \Gamma(t_{i+j-1})|_k \quad, \quad k = 1, 2, \cdots, N_\mathrm{P} \quad, \quad i = 1, 2, \cdots, N_\mathrm{t} - D + 1 \tag{30}$$

where D represents the time window size; $\Gamma(t_{i+j-1})|_k$ is the response vector at measurement points for the $i+j-1$-th time step in the k-th flight case; and $\mathrm{E} \in \mathbb{R}^{D \times 1}$ reads a convolutional kernel. This kernel exhibits temporal shift-invariance and consists of either fixed or trainable parameters. By sliding the kernel across different time steps, the model effectively performs temporal pooling over the original response sequence. By regarding the synthesized responses as inputs and feature coefficients as outputs, the data-driven module can model the causal relationship between structural responses and aerodynamic loads. Time-delay units yield a synthesized response sequence containing $N_\mathrm{t} - D + 1$ samples for each flight case. To maintain dimensional consistency between inputs and outputs, the first $N_\mathrm{t} - D + 1$ samples of features coefficient are retained. Additionally, to enhance model robustness against measurement noise, Gaussian noises with different intensities are added to the training responses. Both synthesized responses and feature coefficients are normalized to improve training efficiency and stability by

$$\widetilde{\Gamma}_\mathrm{N}^{(j)}(t_i)|_k = \frac{\widetilde{\Gamma}^{(j)}(t_i)|_k - \min\{\widetilde{\Gamma}^{(j)}(t)\}}{\max\{\widetilde{\Gamma}^{(j)}(t)\} - \min\{\widetilde{\Gamma}^{(j)}(t)\}} \cdot \Lambda_\mathrm{N}^{(j)}(t_i)|_k = \frac{\Lambda^{(j)}(t_i)|_k - \min\{\Lambda^{(j)}(t)\}}{\max\{\Lambda^{(j)}(t)\} - \min\{\Lambda^{(j)}(t)\}} \tag{31}$$

where the subscript 'N' indicates the normalized data.

Given that the ROM for aerodynamic loads, modal space projection and Newmark-based CSD simulations are all linear transformations, the MLP model is well suited to map structural responses to feature coefficients. As shown in Fig. 3, the MLP is composed of an input layer, multiple hidden layers and an output layer. The forward propagation between layers follows

$$\begin{aligned} \mathbf{Y}_1 &= \mathrm{O}(\mathbf{w}_i \widetilde{\Gamma}_\mathrm{N} + \theta_i) \\ \mathbf{Y}_i &= \mathrm{O}(\mathbf{w}_i \mathbf{Y}_{i-1} + \theta_i), \quad 1 \le i \le N_\mathrm{h} \\ \Lambda_{\mathrm{N,\,P}} &= \mathbf{w}_{N_\mathrm{h}+1} \mathbf{Y}_{N_\mathrm{h}} + \theta_{N_\mathrm{h}+1} \end{aligned} \tag{32}$$

where the normalized synthesized responses ($\widetilde{\Gamma}_\mathrm{N}$) are regarded as the inputs; $\mathbf{Y}_i$ represents the output of the i-th layer, which is equal to the input of the $i+1$-th layer; $\Lambda_{\mathrm{N,\,P}}$ denotes final output corresponding to normalized feature coefficients; N_h is the number of hidden

layers; $\mathbf{w}_i$ and θ_i indicate the trainable weight matrix and bias vector of the i-th layer; and $O(\times)$ embodies the activation function. The predicted feature coefficients (Λ_P) are obtained by inverse-normalizing the network outputs ($\Lambda_{N,P}$).

In the physics-based module, aerodynamic loads are reconstructed from the predicted feature coefficients obtained through the data-driven module, enabling subsequent prediction of modal loads ($\mathbb{F}_P$)

$$\mathbb{F}_P \approx \mathbf{\Phi}^T(\widehat{\mathbf{U}}_A \Lambda_P + \overline{\mathbb{F}}) \tag{33}$$

Modal responses are then calculated in the modal space using the Newmark method, and structural responses at measurement points are recovered through modal superposition. Synthetic responses under predicted aerodynamic loads are then generated using Eq. (30), completing the forward workflow of the aerodynamic response analysis. If the convolution kernel in the time-delay units is fixed, the mapping between modal loads and synthetic responses in the physics-based module can be precomputed to form a transfer matrix (**T**), accelerating response prediction, namely

$$\widetilde{\Gamma}_P = \mathbf{T}\,\mathbb{F}_P = \mathbf{T}\left[\mathbf{\Phi}^T(\widehat{\mathbf{U}}_A \Lambda_P + \overline{\mathbb{F}})\right] \tag{34}$$

It is important to note that noise-free responses are used in Eq. (34) to ensure strict adherence to physical laws. This framework is particularly effective for time-transient flight cases, where CFD and CSD simulations are required. For quasi-steady flight cases (e.g., cruising), the system can be approximated as equilibrium or quasi-equilibrium. In such cases, steady-state fluid and static structural simulations are involved, making time-delay units unnecessary. The response prediction (taking displacements as an example) can be simplified as

$$\widetilde{\Gamma}_P = \Gamma_P = \mathbf{T}\,\mathbb{F}_P = \widehat{\mathbf{\Phi}}\widehat{\mathbf{K}}^{-1}\mathbb{F}_P = \widehat{\mathbf{\Phi}}\widehat{\mathbf{K}}^{-1}\left[\mathbf{\Phi}^T(\widehat{\mathbf{U}}_A \Lambda_P + \overline{\mathbb{F}})\right] \tag{35}$$

The PDNN loss function is defined as the mean squared error (MSE) between the predicted and measured synthesized responses

$$L_{Phy} = \sum_{i=1}^{N_t}\sum_{j=1}^{N_m}\sum_{k=1}^{N_P}\|\,\widetilde{\Gamma}^{(j)}(t_i)|_k - \widetilde{\Gamma}_P^{(j)}(t_i)|_k\,\|_2^2 \tag{36}$$

This completes the forward propagation process of the PDNN, where structural responses at measurement points sequentially pass through the data-driven and physics-based modules to define the loss function. During backpropagation, gradients of the loss function with respect to all trainable parameters are computed via automatic differentiation. Trainable parameters are updated by the Adam optimizer to minimize the loss function.

Notably, PDNN adopts a self-supervised learning framework, as training does not require labeled feature coefficients of aerodynamic loads. This enables direct training using experimentally measured responses, eliminating dependence on labeled aerodynamic loads that are often difficult to obtain, thereby enhancing practical applicability. When simulated data is available, a traditional supervised learning framework can also be applied, where the loss function is defined by the MSE between the predict and labeled feature coefficients, i.e.,

$$L_{Dat} = \sum_{i=1}^{N_t}\sum_{j=1}^{N_m}\sum_{k=1}^{N_P}\|\,\Lambda_N^{(j)}(t_i)|_k - \Lambda_{N,P}^{(j)}(t_i)|_k\,\|_2^2 \tag{37}$$

Eq. (37) can be regarded as a purely data-driven neural network. Furthermore, Eqs. (36) and (37) can be combined into a semi-supervised framework, hybrid physics-data-driven loss function can be defined by combining the physics-consistent self-supervised term with the data-driven supervised term, i.e.,

$$L_{Hyb} = \alpha\sum_{i=1}^{N_t}\sum_{j=1}^{N_m}\sum_{k=1}^{N_P}\|\,\widetilde{\Gamma}^{(j)}(t_i)|_k - \widetilde{\Gamma}_P^{(j)}(t_i)|_k\,\|_2^2 + \beta\sum_{i=1}^{N_t}\sum_{j=1}^{N_m}\sum_{k=1}^{N_P}\|\,\Lambda_N^{(j)}(t_i)|_k - \Lambda_{N,P}^{(j)}(t_i)|_k\,\|_2^2 \tag{38}$$

where $\alpha = \frac{1}{\sum_{i=1}^{N_t}\sum_{j=1}^{N_m}\sum_{k=1}^{N_P}\|\widetilde{\Gamma}^{(j)}(t_i)|_k\|_2^2}$ and $\beta = \frac{1}{\sum_{i=1}^{N_t}\sum_{j=1}^{N_m}\sum_{k=1}^{N_P}\|\Lambda_N^{(j)}(t_i)|_k\|_2^2}$ are weighting coefficients. Comparative validation studies will evaluate the performance of these three loss functions in terms of aerodynamic load inversion performance.

7. Interval estimation of aerodynamic loads under structural field uncertainties

The aerodynamic load inversion in Section III is developed under deterministic assumptions, where structural parameters such as material properties, geometric dimensions and boundary conditions are regarded as precisely known and invariant. In practice, however, this idealization rarely holds, as structural uncertainties are unavoidable and may vary spatially. Existing studies have primarily adopted two methods for uncertainty analysis: probabilistic methods based on statistical theory and non-probabilistic methods based on bounded sets [44,45]. For aircraft structures, the limited availability of samples makes it difficult to accurately determine probabilistic distributions of uncertain parameters. Thus, this section employs an interval-based non-probabilistic model, which represents uncertainties by their upper and lower boundaries instead of probabilistic distributions.

8. Interval Karhunen-Loève decomposition (IKLD) for structural field uncertainties

Considering the non-uniformity and boundedness of structural parameters, the interval field model is employed to describe uncertainties, as illustrated in Fig. 4. For each structural element, the material properties are characterized by the parameter values at its centroid. Thus, the interval filed model can be discretized and indicated by the interval model at of each element, namely

$$\mathbf{P}(\boldsymbol{\Theta}_i) \in \mathbf{P}^{\mathrm{I}}(\boldsymbol{\Theta}_i) = \left[\underline{\mathbf{P}}(\boldsymbol{\Theta}_i) , \overline{\mathbf{P}}(\boldsymbol{\Theta}_i) \right] \quad , \quad i = 1, 2, \cdots, N_{\mathrm{e}} \tag{39}$$

where $\mathbf{P}(*)$ is the vector of uncertain parameter; the superscript "I" means the interval terms; $\underline{\mathbf{P}}(*)$ and $\overline{\mathbf{P}}(*)$ are the lower and upper boundary functions; and N_{e} is the number of structural elements. The boundary functions can be further decomposed into center and radius functions, i.e.,

$$\mathbf{P}^{\mathrm{c}}(\boldsymbol{\Theta}_i) = \frac{\underline{\mathbf{P}}(\boldsymbol{\Theta}_i) + \overline{\mathbf{P}}(\boldsymbol{\Theta}_i)}{2} \cdot \mathbf{P}^{\mathrm{r}}(\boldsymbol{\Theta}_i) = \frac{\overline{\mathbf{P}}(\boldsymbol{\Theta}_i) - \underline{\mathbf{P}}(\boldsymbol{\Theta}_i)}{2} \tag{40}$$

Accordingly, the interval field function can be given by

$$\mathbf{P}(\boldsymbol{\Theta}_i) = \mathbf{P}^{\mathrm{c}}(\boldsymbol{\Theta}_i) + \mathbf{P}^{\mathrm{r}}(\boldsymbol{\Theta}_i) \circ \xi(\boldsymbol{\Theta}_i) \quad , \quad \xi(\boldsymbol{\Theta}_i) \in [-1, 1] \tag{41}$$

where '∘' means the Hadamard product, namely element-wise multiplication.

To ensure spatial continuity of uncertain parameters, the interval model must satisfy specific spatial correlation properties. The covariance function between any two elements is defined as

$$\mathbf{X}(\boldsymbol{\Theta}_i, \boldsymbol{\Theta}_j) = Cov\left[\mathbf{P}(\boldsymbol{\Theta}_i), \mathbf{P}(\boldsymbol{\Theta}_j)\right] = \rho\left[\mathbf{P}(\boldsymbol{\Theta}_i), \mathbf{P}(\boldsymbol{\Theta}_j)\right]\mathbf{P}^{\mathrm{r}}(\boldsymbol{\Theta}_i)\mathbf{P}^{\mathrm{r}}(\boldsymbol{\Theta}_j) = \rho(\boldsymbol{\Theta}_i, \boldsymbol{\Theta}_j)\mathbf{P}^{\mathrm{r}}(\boldsymbol{\Theta}_i)\mathbf{P}^{\mathrm{r}}(\boldsymbol{\Theta}_j) \tag{42}$$

where $\rho(\boldsymbol{\Theta}_i, \boldsymbol{\Theta}_j) = \rho\left[\mathbf{P}(\boldsymbol{\Theta}_i), \mathbf{P}(\boldsymbol{\Theta}_j)\right]$ is the autocorrelation coefficient, determined through experimental samples combined with semi-empirical formulas. The autocorrelation function matrix of the interval filed with the most commonly used exponential decay form is given by [46]

$$\mathbf{R} = \begin{bmatrix} \rho(\boldsymbol{\Theta}_1, \boldsymbol{\Theta}_1) & \rho(\boldsymbol{\Theta}_1, \boldsymbol{\Theta}_2) & \cdots & \rho(\boldsymbol{\Theta}_1, \boldsymbol{\Theta}_{N_{\mathrm{e}}}) \\ \rho(\boldsymbol{\Theta}_2, \boldsymbol{\Theta}_1) & \rho(\boldsymbol{\Theta}_2, \boldsymbol{\Theta}_2) & \cdots & \rho(\boldsymbol{\Theta}_2, \boldsymbol{\Theta}_{N_{\mathrm{e}}}) \\ \vdots & \vdots & \ddots & \vdots \\ \rho(\boldsymbol{\Theta}_{N_{\mathrm{e}}}, \boldsymbol{\Theta}_1) & \rho(\boldsymbol{\Theta}_{N_{\mathrm{e}}}, \boldsymbol{\Theta}_2) & \cdots & \rho(\boldsymbol{\Theta}_{N_{\mathrm{e}}}, \boldsymbol{\Theta}_{N_{\mathrm{e}}}) \end{bmatrix} \quad , \quad \rho(\boldsymbol{\Theta}_i, \boldsymbol{\Theta}_j) = \exp\left(\frac{\| \boldsymbol{\Theta}_i - \boldsymbol{\Theta}_j \|}{\mathbf{l}}\right) \tag{43}$$

where $\mathbf{l}$ represents the correlation length, governing the degree of spatial fluctuation. Larger $\mathbf{l}$ indicates smoother fluctuations. When the boundary functions are constant and the covariance function depends only on spatial distance, the interval field is classified as isotropic.

Direct uncertainty analysis of the spatially varying interval field model is computationally expensive. To reduce this complexity, an interval Karhunen-Loève decomposition (IKLD) is employed [47], inspired by the ROM for aerodynamic loads. The interval field can be approximated by retaining the dominant terms while truncating negligible ones, i.e.,

$$\mathbf{P}_k(\boldsymbol{\Theta}_i) \approx \mathbf{P}_k^{\mathrm{c}}(\boldsymbol{\Theta}_i) + \sum_{m=1}^{N_{\mathrm{KL}}} \mathbf{P}^{\mathrm{r}}(\boldsymbol{\Theta}_i) \sqrt{\lambda_{k,(m)}} \, \boldsymbol{\varphi}_{k,(m,i)} \, \delta_{k,(m)} \tag{44}$$

where the subscript k denotes the k-th uncertain parameter; $\delta_{k,(m)} \in [-1, 1]$ is independent standard interval variables satisfying $\sum_{m=1}^{N_{\mathrm{KL}}} \delta_{k,(m)} \leq 1$; N_{KL} reads the truncation order, determined similarly to Eq. (22); λ_k and $\boldsymbol{\varphi}_k$ are eigenvalues and eigenvectors obtained from the eigen-decomposition of the autocorrelation function matrix $\mathbf{R}_k$, namely
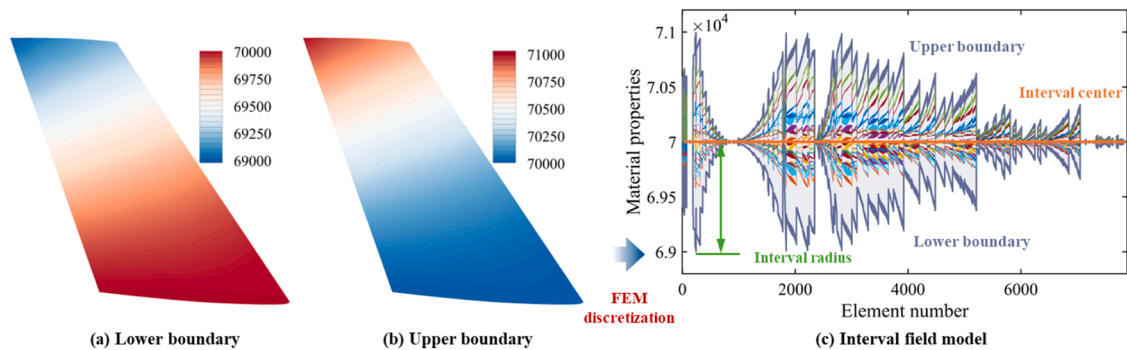

Fig 4. Schematic of the interval field model.

$$\mathbf{R}_k = \sum_{m=1}^{N_s} \lambda_{k,(m)} \boldsymbol{\varphi}_{k,(m,\,:\,)} \boldsymbol{\varphi}_{k,(m,\,:\,)}^{\mathrm{T}} \tag{45}$$

where $\lambda_{k,(m)}$ is the m-th eigenvalue; and $\boldsymbol{\varphi}_{k,(m,i)}$ is the i-th component of the m-th eigenvector. The interval field is thus expressed as a linear combination of independent standard interval variables and deterministic eigenfunctions associated with structural elements, enabling efficient characterization with only a limited number of interval variables.

When $\Theta = 1$, the interval field model is reduced into a one-dimensional standard interval model. When $\Theta > 1$, the interval field model is reduced into a standard spherical model, which can be transformed into an interval model via generalized spherical co-ordinates, namely

$$\begin{cases} \begin{cases} \delta_{k,1} = r\cos\phi_1, \\ \delta_{k,2} = r\sin\phi_1\cos\phi_2, \\ \delta_{k,2} = r\sin\phi_1\sin\phi_2\cos\phi_3, \\ \vdots \\ \delta_{k,N_{\mathrm{KL}}-1} = r\sin\phi\sin\phi_2\cdots\sin\phi_{N_{\mathrm{KL}}-2}\cos\phi_{N_{\mathrm{KL}}-1}, \\ \delta_{k,N_{\mathrm{KL}}} = r\sin\phi\sin\phi_2\cdots\sin\phi_{N_{\mathrm{KL}}-2}\sin\phi_{N_{\mathrm{KL}}-1}, \end{cases} \\ \sum_{m=1}^{N_{\mathrm{KL}}} \delta_{k,m} \leq 1 \end{cases} \tag{46}$$

where $r \in [0, 1]$, $\phi_1, \phi_2, \cdots, \phi_{\Theta-2} \in [0, \pi]$ and $\phi_{\Theta-1} \in [0, 2\pi]$ represent the radius, polar angle, and azimuthal angle in spherical co-ordinates, respectively, all expressed as interval variables. By aggregating interval variables across all dimensions, the uncertain parameters can be uniformly expressed as a vector, namely, $\mathbf{b} = [r, \phi_1, \phi_2, \cdots, \phi_{\Theta-2}, \phi_{\Theta-1}, \cdots]$, where N_{u} is the number of interval variables. In summary, this approach transforms the interval field into a finite-dimensional interval model, significantly reducing computational complexity in subsequent uncertainty analysis.

9. Interval boundary estimation of aerodynamic loads based on adaptive Kriging surrogate model (AKSM)

When structural uncertainties are introduced, the stiffness, mass, damping and modal matrices in the PDNN model become interval matrices. Accordingly, the predicted feature coefficients are also interval variables. In this case, uncertainty propagation should be involved to determine the interval boundaries of aerodynamic loads. A common approach is the Monte Carlo method, which samples numerous interval variables ($\mathbf{b}^{\mathrm{M}} = \{\mathbf{b}^1, \mathbf{b}^2, \cdots, \mathbf{b}^{N_{\mathrm{M}}}\}$) and maps them to structural parameters ($\mathbf{P}^{\mathrm{M}} = \{\mathbf{P}^1, \mathbf{P}^2, \cdots, \mathbf{P}^{N_{\mathrm{M}}}\}$) via Eq. (46). For each sample, deterministic aerodynamic load inversion is performed to get the feature coefficients ($\Lambda_{\mathrm{P}}^{\mathrm{M}} = \{\Lambda_{\mathrm{P}}^1, \Lambda_{\mathrm{P}}^2, \cdots, \Lambda_{\mathrm{P}}^{N_{\mathrm{M}}}\}$). The upper and lower boundaries of the aerodynamic loads can be determined by

$$\overline{\mathbb{F}}_{\mathrm{P}} \approx \max\left\{\mathbb{F}_{\mathrm{P}}^{N_{\mathrm{M}}} \middle| \mathbb{F}_{\mathrm{P}}^{N_{\mathrm{M}}} \approx \boldsymbol{\Phi}^{\mathrm{T}}\left(\widehat{\mathbf{U}}_{\mathbf{A}}\Lambda_{\mathrm{P}}^{N_{\mathrm{M}}} + \overline{\mathbb{F}}\right)\right\} \cdot \underline{\mathbb{F}}_{\mathrm{P}} \approx \min\left\{\mathbb{F}_{\mathrm{P}}^{N_{\mathrm{M}}} \middle| \mathbb{F}_{\mathrm{P}}^{N_{\mathrm{M}}} \approx \boldsymbol{\Phi}^{\mathrm{T}}\left(\widehat{\mathbf{U}}_{\mathbf{A}}\Lambda_{\mathrm{P}}^{N_{\mathrm{M}}} + \overline{\mathbb{F}}\right)\right\} \tag{47}$$

Although straightforward to implement, this method is computationally inefficient, as many samples do not contribute to the boundary results. Considering that the ROM for aerodynamic load is linear, the interval boundaries of aerodynamic loads are directly governed by the boundaries of the feature coefficients. Thus, instead of large-scale sampling, a more efficient strategy is to approximate these extrema through surrogate modeling. To this end, an adaptive Kriging surrogate model (AKSM) [48] is established for uncertainty propagation. The Kriging surrogate model for the feature coefficients with respect to interval variables is defined as

$$\Lambda_{\mathrm{P}} = [\mathbf{p}(\mathbf{b})]^{\mathrm{T}}\boldsymbol{\beta} + \mathbf{w}(\mathbf{b}) \tag{48}$$

where $\mathbf{p}(\mathbf{b}) = [\mathbf{p}_1(\mathbf{b}), \mathbf{p}_2(\mathbf{b}), \cdots, \mathbf{p}_\zeta(\mathbf{b})]^{\mathrm{T}}$ represents the deterministic linear trend term; $\boldsymbol{\beta}$ reads the corresponding coefficient vector; $\mathbf{w}(\mathbf{b})$ is a zero-mean Gaussian process with covariance $Cov\left[\mathbf{w}\left(\mathbf{b}^j\right), \mathbf{w}\left(\mathbf{b}^k\right)\right] = \lambda^2 S\left(\mathbf{b}^j, \mathbf{b}^k, \boldsymbol{\theta}\right)$; λ^2 is process variance; $S\left(\mathbf{b}^j, \mathbf{b}^k, \boldsymbol{\theta}\right) = \exp\left(-\sum_{z=1}^Z \boldsymbol{\theta}_z\left(\mathbf{b}^j - \mathbf{b}^k\right)^2\right)$ relates to the correlation function; and $\boldsymbol{\theta}$ refers to the hyperparameters.

Suppose τ samples are initially generated via Latin hypercube sampling (LHS), denoted as $\mathbf{b}^{\boldsymbol{\tau}} = \left[\mathbf{b}^1, \mathbf{b}^2, \cdots, \mathbf{b}^\tau\right]^{\mathrm{T}}$, with feature coefficients $\Lambda_{\mathrm{P}}^{\boldsymbol{\tau}} = \Lambda_{\mathrm{P}}(\mathbf{b}^{\boldsymbol{\tau}}) = \left[\Lambda_{\mathrm{P}}\left(\mathbf{b}^1\right), \Lambda_{\mathrm{P}}\left(\mathbf{b}^2\right), \cdots, \Lambda_{\mathrm{P}}(\mathbf{b}^\tau)\right]^{\mathrm{T}}$. The covariance matrix of these samples is $\mathbf{Y}_{\mathbf{b}}^{\boldsymbol{\tau}} = \left[\lambda^2 S\left(\mathbf{b}^j, \mathbf{b}^k, \boldsymbol{\theta}\right)\right]$ $(j, k = 1, 2, \cdots, \tau)$. Using the Lagrange multiplier method, the predicted mean and variance of the surrogate model is given by

$$\widehat{\Lambda}_{\mathrm{P}}^{(\tau)}(\mathbf{b}) = [\mathbf{p}(\mathbf{b})]^{\mathrm{T}}\widehat{\boldsymbol{\beta}}^{(\tau)} + [\mathbf{y}(\mathbf{b}, \mathbf{b}^{\boldsymbol{\tau}})]^{\mathrm{T}}\left(\mathbf{Y}_{\mathbf{b}}^{\boldsymbol{\tau}}\right)^{-1}\left[\widehat{\Lambda}_{\mathrm{P}}^{\boldsymbol{\tau}} - (\mathbf{p}^{\boldsymbol{\tau}})^{\mathrm{T}}\widehat{\boldsymbol{\beta}}^{(\tau)}\right]$$
$$\mathbf{V}^{2\,(\tau)}(\mathbf{b}) = \lambda^{2\,(\tau)}(\mathbf{b})\left[1 + [\mathbf{u}(\mathbf{b})]^{\mathrm{T}}\left[(\mathbf{p}^{\boldsymbol{\tau}})^{\mathrm{T}}\left(\mathbf{Y}_{\mathbf{b}}^{\boldsymbol{\tau}}\right)^{-1}\mathbf{p}^{\boldsymbol{\tau}}\right]^{-1}\mathbf{u}(\mathbf{b}) - [\mathbf{y}(\mathbf{b}, \mathbf{b}^{\boldsymbol{\tau}})]^{\mathrm{T}}\left(\mathbf{Y}_{\mathbf{b}}^{\boldsymbol{\tau}}\right)^{-1}\mathbf{y}(\mathbf{b}, \mathbf{b}^{\boldsymbol{\tau}})\right] \tag{49}$$

where $\widehat{\beta}^{(\tau)} = \left[(\mathbf{p}^{\tau})^{\mathbf{T}} (\mathbf{Y}_{\mathbf{b}}^{\tau})^{-1} \mathbf{p}^{\tau} \right]^{-1} (\mathbf{p}^{\tau})^{\mathbf{T}} (\mathbf{Y}_{\mathbf{b}}^{\tau})^{-1} \Lambda_{\mathrm{P}}^{\tau}$ denotes the least squares estimation of β; $\mathbf{y}(\mathbf{b}, \mathbf{b}^{\tau}) = \left[\lambda^2 S\left(\mathbf{b}, \mathbf{b}^1, \theta\right), \lambda^2 S\left(\mathbf{b}, \mathbf{b}^2, \theta\right), \cdots, \lambda^2 S\left(\mathbf{b}, \mathbf{b}^{\tau}, \theta\right) \right]^{\mathbf{T}}$ means the correlation vector between $\mathbf{b}$ and $\mathbf{b}^{\tau}$; $\mathbf{p}^{\tau} = \left[\mathbf{p}\left(\mathbf{b}^1\right), \mathbf{p}\left(\mathbf{b}^2\right), \cdots, \mathbf{p}(\mathbf{b}^{\tau}) \right]^{\mathbf{T}}$ indicates the trend term matrix; $\lambda^{2\ (\tau)}(\mathbf{b}) = \frac{1}{\tau} \left[\Lambda_{\mathrm{P}}^{\tau} - \mathbf{p}^{\tau} \widehat{\beta}^{(\tau)} \right]^{\mathbf{T}} (\mathbf{p}^{\tau})^{-1} \left[\Lambda_{\mathrm{P}}^{\tau} - \mathbf{p}^{\tau} \widehat{\beta}^{(\tau)} \right]$ stands for the optimal estimation of variance at the τ-th iteration; and $\mathbf{u}(\mathbf{b}) = (\mathbf{p}^{\tau})^{\mathbf{T}} (\mathbf{Y}_{\mathbf{b}}^{\tau})^{-1} \mathbf{r}(\mathbf{b}) - \mathbf{p}(\mathbf{b})$. The prediction result of the Kriging model follows a normal distribution, i.e., $\Lambda_{\mathrm{P}}^{(\tau)}(\mathbf{b}) \sim \mathrm{N} \left[\widehat{\Lambda}_{\mathrm{P}}^{(\tau)}(\mathbf{b}), \mathbf{V}^{2\ (\tau)}(\mathbf{b}) \right]$.

If the distribution of selected samples is suboptimal, the prediction accuracy of the Kriging surrogate model is insufficient. To refine it, additional samples must be added. Uniform sampling often leads to redundant computations, while focusing only near the current optimum results in local convergence and weak global representation. To balance exploitation and exploration, the Expected Improvement (EI) criterion [49] is employed in this AKSM framework. By integrating the predicted mean and variance, the points that both improve the current extrema and lie in regions of high uncertainty will be identified, thereby enabling efficient refinement of the surrogate model within limited computational budgets. Guided by EI criterion, new samples are adaptively allocated near the extrema of feature coefficients, facilitating progressive convergence toward the interval boundaries. Denote the minimum and maximum feature coefficients at the τ-th iteration as $\Lambda_{\mathrm{P},\ \min}^{\tau} = \min \left\{ \Lambda_{\mathrm{P}}\left(\mathbf{b}^1\right), \Lambda_{\mathrm{P}}\left(\mathbf{b}^2\right), \cdots, \Lambda_{\mathrm{P}}(\mathbf{b}^{\tau}) \right\}$ and $\Lambda_{\mathrm{P},\ \max}^{\tau} = \max \left\{ \Lambda_{\mathrm{P}}\left(\mathbf{b}^1\right), \Lambda_{\mathrm{P}}\left(\mathbf{b}^2\right), \cdots, \Lambda_{\mathrm{P}}(\mathbf{b}^{\tau}) \right\}$. For the lower boundary of feature coefficients, the EI function is defined as the potential enhancement between the current minimum and the prediction at a new sample ($\Lambda_{\mathrm{P}}(\mathbf{b})$), namely

$$\mathrm{EI}_{\min}^{(\tau)}(\mathbf{b}) = \mathrm{E} \left\{ \max \left[\Lambda_{\mathrm{P},\ \min}^{\tau} - \Lambda_{\mathrm{P}}(\mathbf{b}) - \chi, 0 \right] \right\} \tag{50}$$

where χ is a bias term preventing premature convergence. Based on the normality of Kriging predictions, the EI function can be analyzed by

$$\mathrm{EI}_{\min}^{(\tau)}(\mathbf{b}) = \begin{cases} \left[\Lambda_{\mathrm{P},\ \min}^{\tau} - \widehat{\Lambda}_{\mathrm{P}}^{(\tau)}(\mathbf{b}) - \chi \right] \Phi \left[\dfrac{\Lambda_{\mathrm{P},\ \min}^{\tau} - \widehat{\Lambda}_{\mathrm{P}}^{(\tau)}(\mathbf{b}) - \chi}{\mathbf{V}^{(\tau)}(\mathbf{b})} \right] + \mathbf{S}_i^{(\tau)}(\mathbf{b}) \phi \left[\dfrac{\Lambda_{\mathrm{P},\ \min}^{\tau} - \widehat{\Lambda}_{\mathrm{P}}^{(\tau)}(\mathbf{b}) - \chi}{\mathbf{V}^{(\tau)}(\mathbf{b})} \right] &, \mathbf{V}^{(\tau)}(\mathbf{b}) > 0 \\ 0 &, \mathbf{V}^{(\tau)}(\mathbf{b}) = 0 \end{cases} \tag{51}$$

where $\Phi(*)$ and $\phi(*)$ represent the cumulative distribution function and probability density function, respectively. Similarly, the EI function for the upper boundary of feature coefficients is defined as:

$$\mathrm{EI}_{\max}^{(\tau)}(\mathbf{b}) = \mathrm{E} \left\{ \max \left[\Lambda_{\mathrm{P}}(\mathbf{b}) - \Lambda_{\mathrm{P},\ \max}^{\tau} - \chi, 0 \right] \right\} \tag{52}$$

with its analytical expression given by

$$\mathrm{EI}_{\max}^{(\tau)}(\mathbf{b}) = \begin{cases} \left[\Lambda_{\mathrm{P}}(\mathbf{b}) - \Lambda_{\mathrm{P},\ \max}^{\tau} - \chi \right] \Phi \left[\dfrac{\Lambda_{\mathrm{P}}(\mathbf{b}) - \Lambda_{\mathrm{P},\ \max}^{\tau} - \chi}{\mathbf{V}^{(\tau)}(\mathbf{b})} \right] + \mathbf{S}_i^{(\tau)}(\mathbf{b}) \phi \left[\dfrac{\Lambda_{\mathrm{P}}(\mathbf{b}) - \Lambda_{\mathrm{P},\ \max}^{\tau} - \chi}{\mathbf{V}^{(\tau)}(\mathbf{b})} \right] &, \mathbf{V}^{(\tau)}(\mathbf{b}) > 0 \\ 0 &, \mathbf{V}^{(\tau)}(\mathbf{b}) = 0 \end{cases} \tag{53}$$

By maximizing $\mathrm{EI}_{\min}^{(\tau)}(\mathbf{b})$ and $\mathrm{EI}_{\max}^{(\tau)}(\mathbf{b})$, two new samples ($\mathbf{b}_{\min}^{(\tau)}$ and $\mathbf{b}_{\max}^{(\tau)}$) are added to the current selected samples to yield an updated
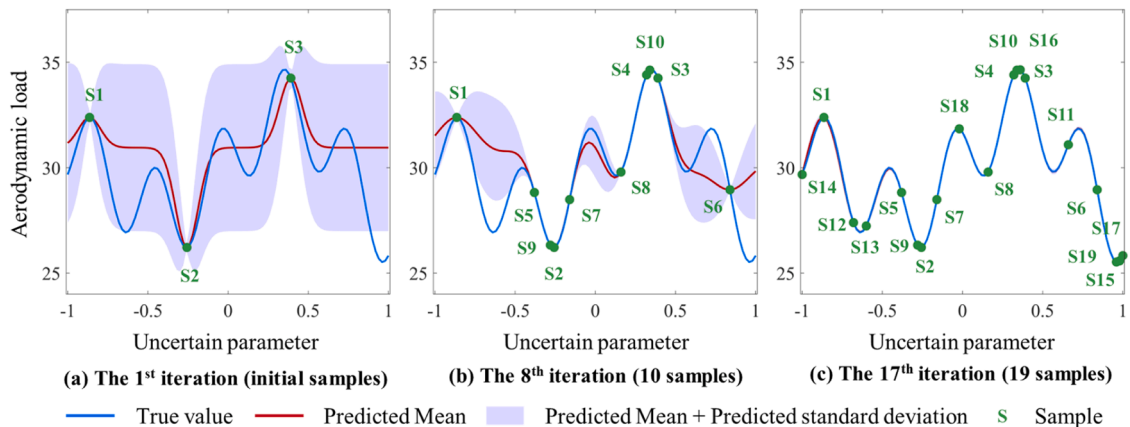

Fig 5. Schematic of the AKSM framework.

set $\mathbf{b}^{\tau+1} = \left[\mathbf{b}^1, \mathbf{b}^2, \cdots, \mathbf{b}^\tau, \mathbf{b}_{\min}^{(\tau)}, \mathbf{b}_{\max}^{(\tau)}\right]^{\mathrm{T}}$, completing one adaptive iteration. The process terminates when the following convergence criterion is met

$$\max\left\{ \| \mathbf{b}_{\min}^{(\tau)} - \mathbf{b}|_{\Lambda_{\mathrm{P},\min}^\tau} \|, \| \mathbf{b}_{\max}^{(\tau)} - \mathbf{b}|_{\Lambda_{\mathrm{P},\max}^\tau} \| \right\} \le \varepsilon \tag{54}$$

where ε is a predefined tolerance. Upon convergence, genetic algorithms can be used to optimize the upper and lower boundaries of the feature coefficients. As this process no longer requires neural network training, computational efficiency is greatly enhanced. Fig. 5 illustrates the adaptive sample collocation process for a one-dimensional uncertain parameter, where the interval boundaries of the aerodynamic load gradually converge to the true value as sampling progresses.

10. Numerical and experimental validations

A hybrid physics-data-based reduced-order modeling framework has been developed for aerodynamic load inversion under structural field uncertainties. As illustrated in Fig. 6, the workflow consists of four core steps: ROM for aerodynamic loads (Section III.A), IKLM for structural field uncertainties (Section IV.A), PDNN for aerodynamic load inversion (Section III.B) and AKSM for interval boundary estimation (Section IV.B). The first two can be regarded as the preparatory stage, the third includes learning and deployment stages, and the fourth calls the third in each iteration. The ultimate goal is to estimate the interval boundaries of aerodynamic loads. In this section, the proposed method will be validated through both numerical and experimental examples. The numerical case will demonstrate the overall methodology, while the experimental case highlights its effectiveness by comparing the inversion results with wind tunnel data.

11. A wing structure

This section focuses on the wing structure (Fig. 7 (a)) to investigate aerodynamic load inversion under both deterministic and field uncertainty parameters. The fluid and structural meshes of the wing are displayed in Fig. 7 (b) and (c), respectively. In the CFD simulations, the flight speed ranges from 0.3 to 0.8 Ma, the angle of attack varies from 0° to 15°, and the Reynolds number ranges from 4.25×10^6 to 1.133×10^7. In the CSD simulations, the elastic modulus of the skin and beam-rib structures are treated as structural field uncertainties. For deterministic inversion, the spatial distribution of the elastic modulus is depicted in Fig. 8 (a). For the uncertainty-oriented inversion, the elastic modulus is modeled as an interval field with a uniform center value of 70 GPa assigned to each structural element, the corresponding interval radius and boundaries are displayed in Fig. 8 (b). In both cases, the material density is set to 2700 g/cm³ and Poisson's ratio to 0.33. By integrating CFD and CSD simulations, strain responses at the strain gauge positions indicated in Fig. 7 (c) are computed and used as measurements for aerodynamic load inversion.
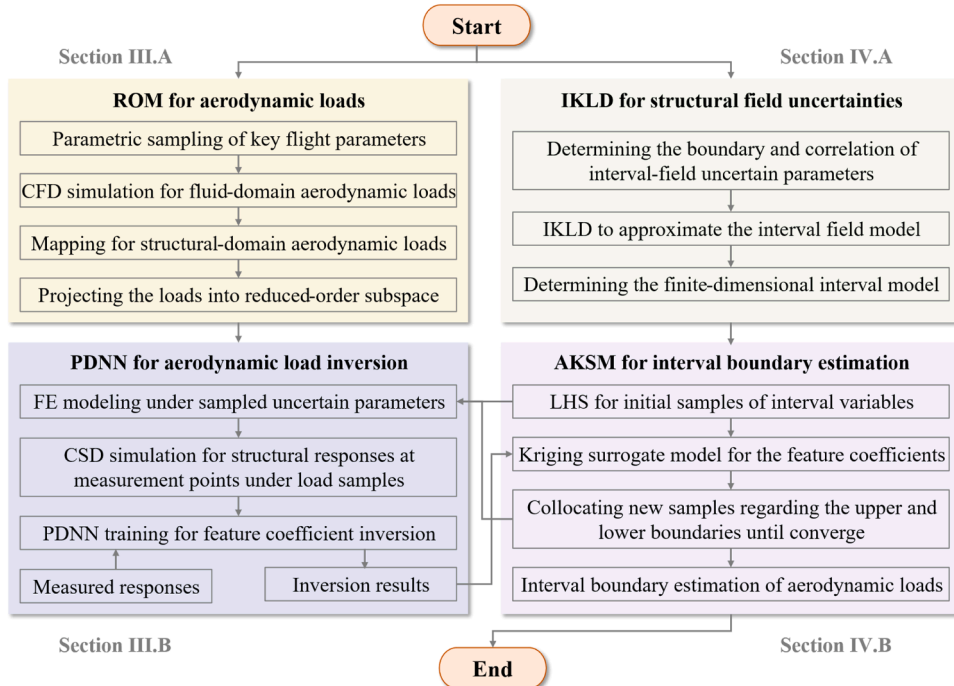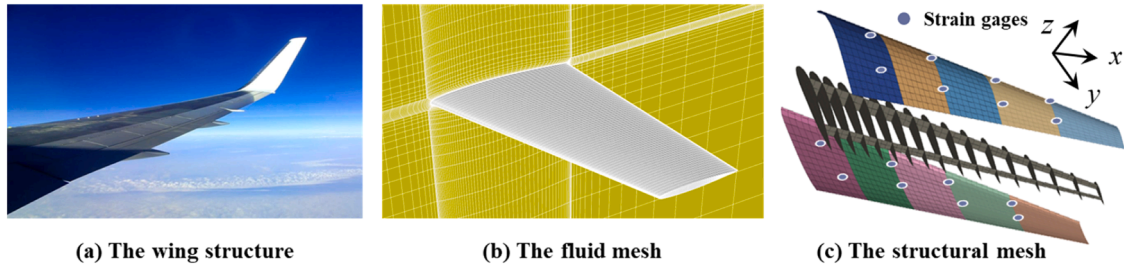

Fig 6. Workflow for the proposed methodology.

(a) The wing structure   (b) The fluid mesh   (c) The structural mesh

Fig 7. Schematic of the wing structure.

The ROM for aerodynamic loads is first constructed. LHS is employed to uniformly sample flight parameters across their defined domain, generating a dataset of 200 aerodynamic load cases, as shown in Fig. 9 (a). For each set of sampled flight parameters, CFD simulations combined with aerodynamic load mapping techniques are conducted to obtain aerodynamic load snapshots in the structural domain. PCA is then applied to the snapshot matrix to extract their dominant spatial distribution features in low-dimensional subspaces, along with their mean distribution features. The PCA threshold is set at 99.5% to preserve as much system energy as possible. The ROM results, presented in Fig. 10, demonstrate that retaining only the first six principal components is sufficient to accurately reconstruct the spatial distribution of the aerodynamic loads. Based on the ROM, deterministic aerodynamic load inversion, uncertainty-oriented inversion and the analyses of influence of structural uncertainties on inversion is conducted, yielding some key conclusions.

11.1. Deterministic aerodynamic load inversion

The flight parameters used for the inversion cases are shown in Fig. 9 (b) and (c). Strain responses at the measurement points for PDNN training are simulated using the LHS-sampled flight parameters. To explore the influence of structural parameter distribution on inversion accuracy, two PDNN models are constructed: PDNN 1 is based on the non-uniform elastic modulus distribution shown in Fig. 8 (a), consistent with the parameters used to generate the strain measurements; PDNN 2 is based on the uniform elastic modulus distribution of 70 GPa. The predicted feature coefficients using these two PDNN models are presented in Fig. 11. The "true coefficients" denotes the feature coefficients derived by projecting the true aerodynamic loads into lower-dimensional subspaces. The average relative errors for all inversion cases and for the 9th inversion case (corresponding to the maximum angle of attack at maximum speed) are reported in Table 1. Furthermore, the reconstructed high-dimensional aerodynamic load for the 9th inversion case, as well as their corresponding errors compared to the true distributions are listed in Table 2.

Based on the above results, in can be concluded that: (1) As shown in Fig. 11, the feature coefficients predicted by the two PDNN models closely follow the trends of the true coefficients. Table 1 demonstrates that the PDNN 1 consistently performs better than the PDNN 2 for all orders, indicating that accurate modeling of structural parameters is essential for improving inversion accuracy. (2) Regardless of whether the structural parameters are matched, the inversion errors for low-order feature coefficients are significantly fewer than those for high-order feature coefficients. Thus, the ROM framework may successfully ensure the overall inversion accuracy since the aerodynamic load distribution is dominated by low-dimensional subspaces. (3) Fig. 11 (e) and (f) show that the inversion errors for the first 30 inversion cases are significantly larger than those for the subsequent cases, indicating that aerodynamic load inversion becomes more challenging as the flight speed increases. (4) As illustrated in Table 2, the ROM of aerodynamic loads introduces an average relative error of 2.018%. The average relative errors of reconstructed aerodynamic loads using the feature coefficients predicted by PDNN 1 and PDNN 2 are 2.105% and 2.182%, respectively. Notably, the error distribution of PDNN 1 closely aligns with that based on the true coefficients, whereas PDNN 2 shows larger, more widespread errors. These results further validate the importance of accurate modeling of structural parameters.
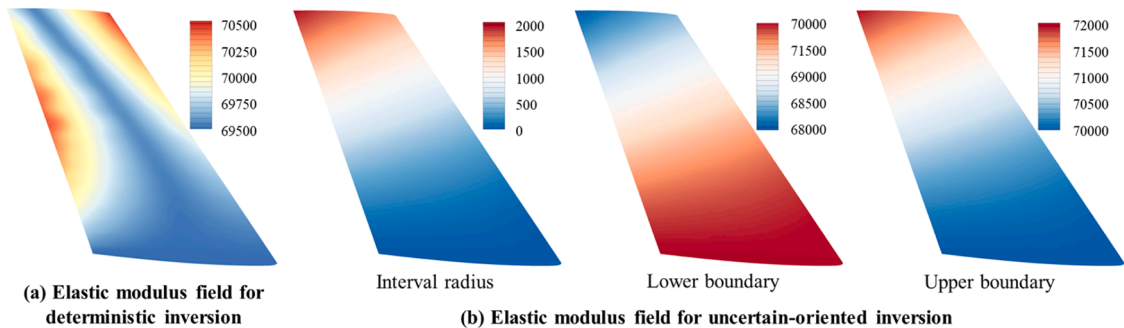

(a) Elastic modulus field for deterministic inversion

Interval radius   Lower boundary   Upper boundary

(b) Elastic modulus field for uncertain-oriented inversion

Fig 8. Spatial distribution of the elastic modulus (Units: MPa).

(a) Parametric sampling   (b) Flight velocities   (c) Flight Angles
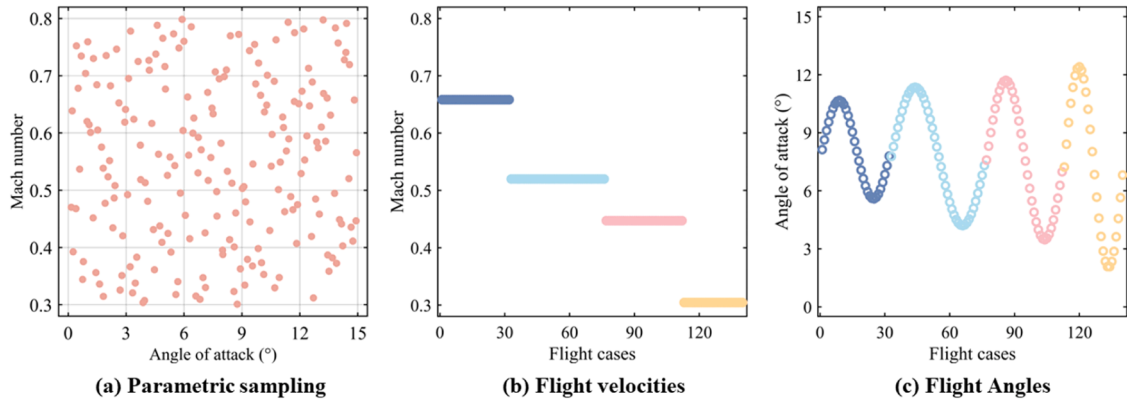
Fig 9. Flight parameters for LHS sampling and inversion cases.

(a) The 1st order (85.769%)   (b) The 2nd order (95.321%)   (c) The 3rd order (97.611%)   (d) The 4th order (99.034%)

(e) The 5th order (99.384%)   (f) The 6th order (99.576%)   (g) Mean feature
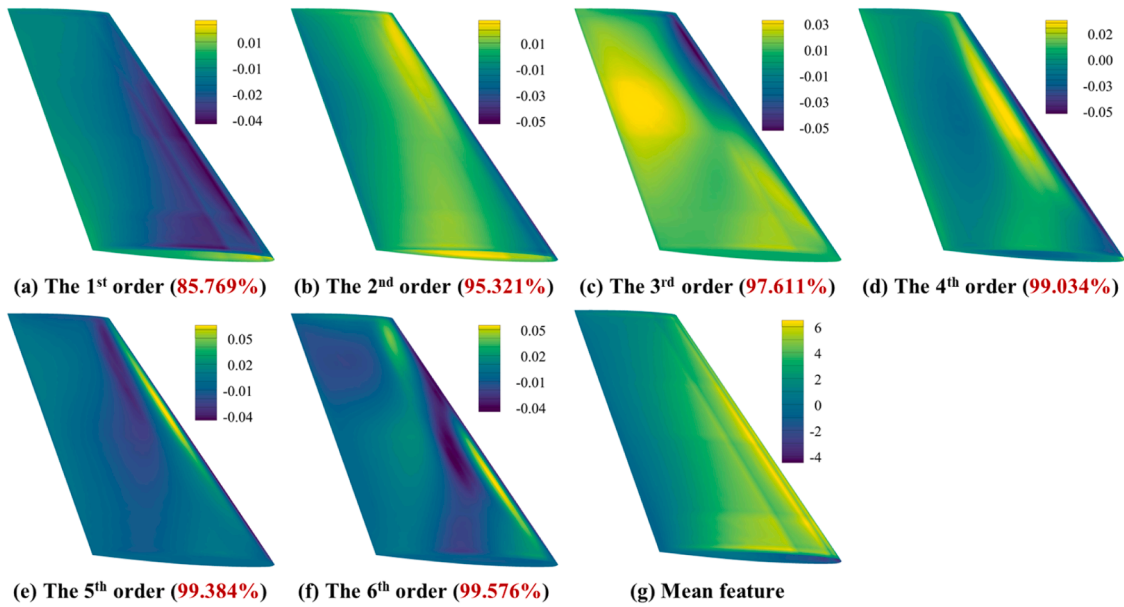
Fig 10. ROM results of aerodynamic loads (Units: N).

11.2. Uncertainty-oriented aerodynamic load inversion

Uncertainty-oriented aerodynamic load identification is conducted based on the interval field model depicted in Fig. 8. Assuming the autocorrelation function has an infinite correlation length (set to 100000), the elastic modulus is fully correlated across all structural elements, yielding the interval field model is reduced into a one-dimensional standard interval model. The interval boundaries of feature coefficients are then estimated using AKSM-based uncertainty propagation, as plotted in Fig. 12. Taking the 9th inversion case as an example, the lower/upper boundary, interval radius and interval fluctuation level of aerodynamic loads reconstructed from the uncertain feature coefficients is presented in Fig. 13.

The key findings are summarized as follows: (1) As shown in Fig. 12, the interval fluctuation of feature coefficients increases with order. Specifically, the interval boundaries of the 1st order (Fig. 12 (a)) are nearly identical, whereas those of the 6th order (Fig. 12 (f)) show clear separation. (2) Consistent with deterministic inversion results, the interval fluctuation of feature coefficients also increases with flight speed, indicating that uncertainty effects become more pronounced under high-speed conditions. (3) The spatial distributions of the reconstructed upper and lower aerodynamic loads align with those from the ROM. However, the spatial distributions of interval radius are mainly governed by the 5th and 6th order. This suggests that low-order features capture the overall distribution pattern, while higher-order features account for spatial uncertainties. (4) Fig. 13 indicates that the maximum fluctuation level reaches 12%, with most fields fluctuating around 4%. In contrast, the maximum fluctuation in the structural parameter field is only 2%, revealing the accumulation and amplification of uncertainties during the inversion process.
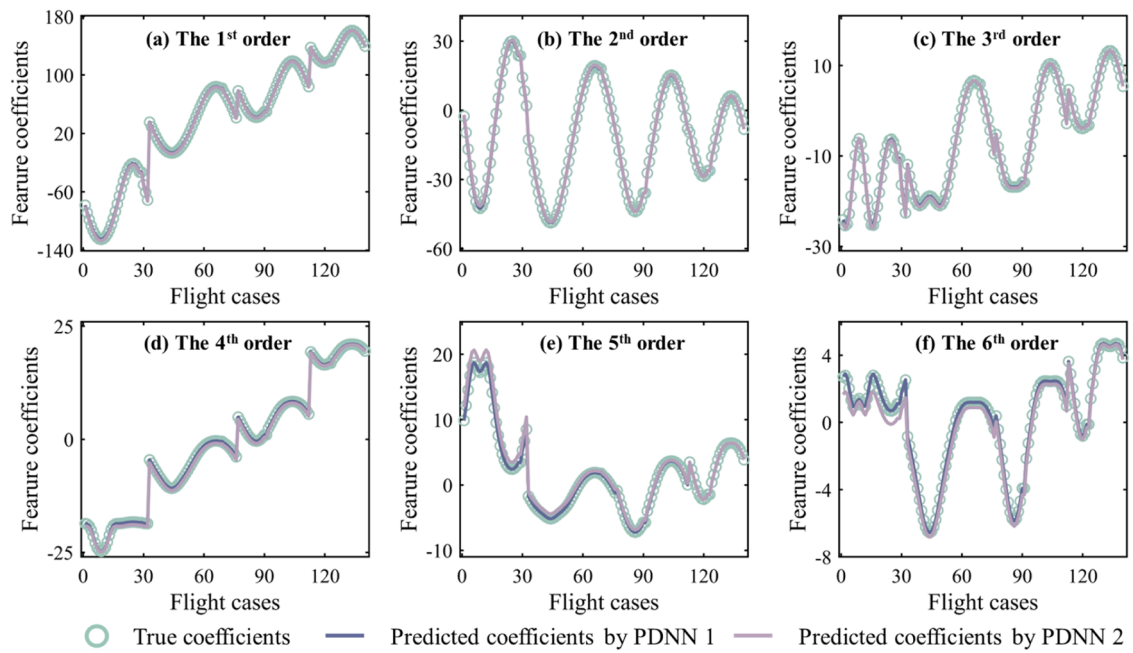
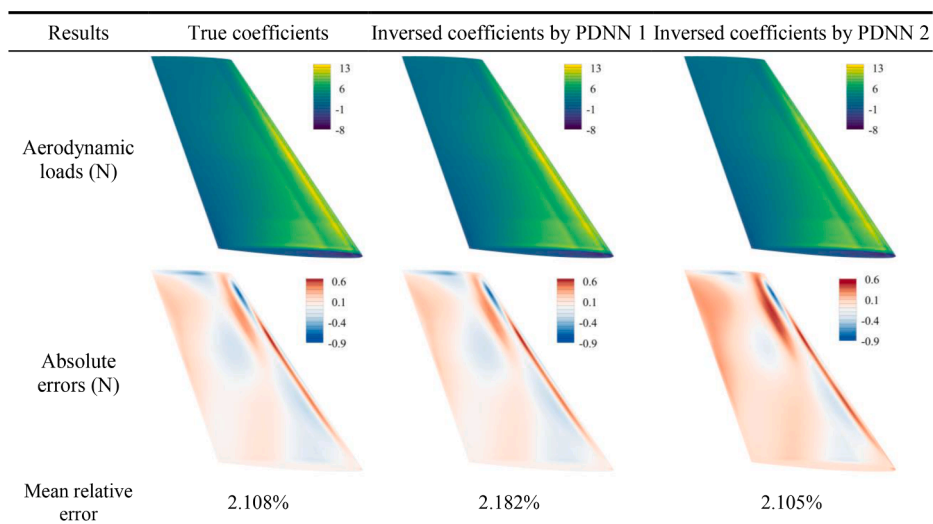**Fig 11.** Feature coefficient results under deterministic inversion.

Table 1
Relative errors under deterministic inversion (Units: %).

Cases	PDNN	The 1st order	The 2nd order	The 3rd order	The 4th order	The 5th order	The 6th order
All cases	PDNN 1	0.007	0.039	0.035	0.157	0.261	0.353
	PDNN 2	5.908	2.666	1.964	39.499	34.292	39.203
The 9th case	PDNN 1	0.027	0.006	0.204	0.152	0.681	3.008
	PDNN 2	1.406	2.378	1.008	0.658	9.978	12.698

Table 2
Reconstructed aerodynamic load results for the 9th case under deterministic inversion.

Results	True coefficients	Inversed coefficients by PDNN 1	Inversed coefficients by PDNN 2
Mean relative error	2.108%	2.182%	2.105%
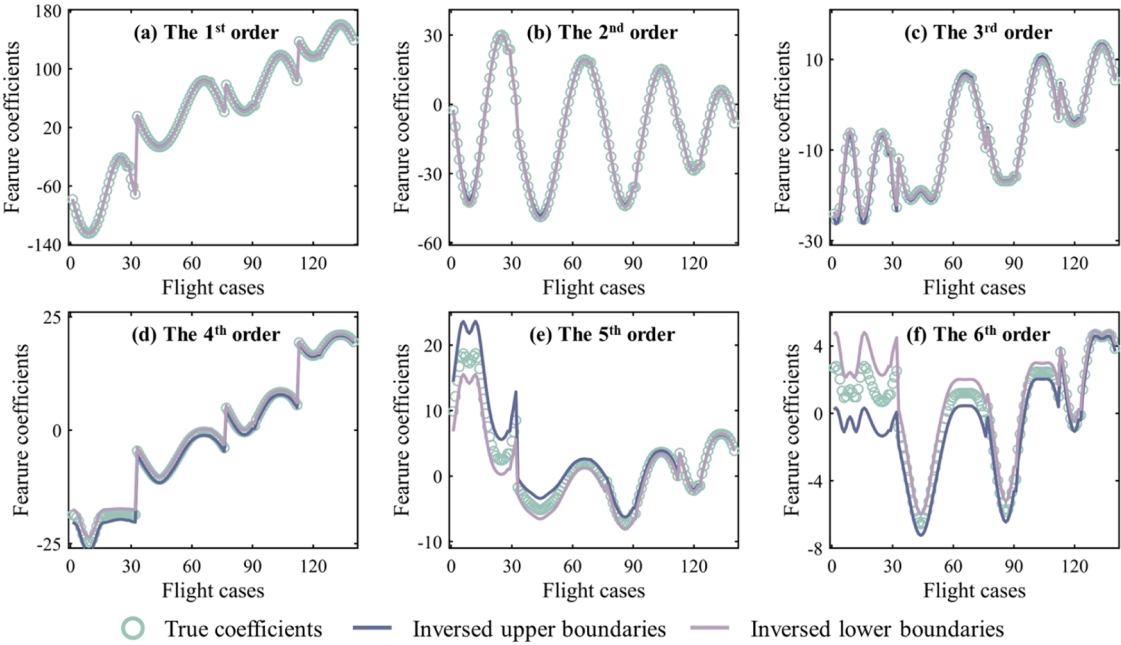
Fig 12. The feature coefficient results under uncertainty-oriented inversion.
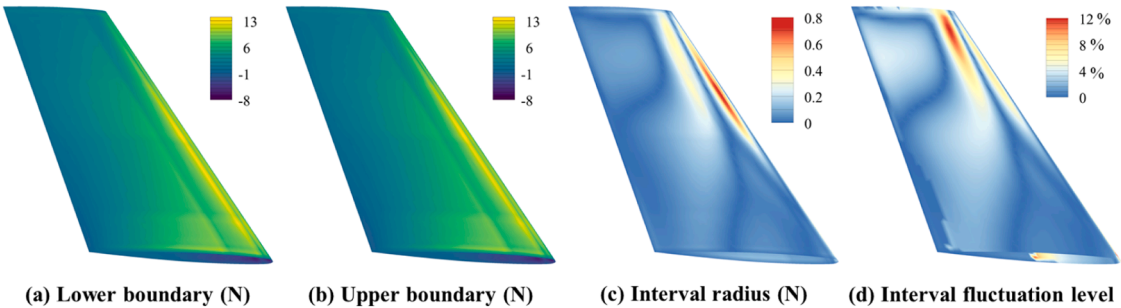
Fig 13. Reconstructed aerodynamic load results for the 9th case under uncertainty-oriented inversion.

11.3. Analyses of influence of structural uncertainties on aerodynamic load inversion

Two key factors will be considered for structural field uncertainties: interval radius and correlation length. For the interval radius, three levels are considered: $0.5 \times$, $1 \times$, and $1.5 \times$ the baseline radius shown in Fig. 8 (b), denoted as Radius 1, 2, and 3, respectively. In this analysis, the correlation length is fixed at 100000, representing different levels of material property dispersion. For the correlation length, values of 100000, 40000, and 2,000 are used, denoted as Length 1, 2, and 3, while the interval radius is held at the baseline level from Fig. 8 (b), simulating different spatial correlations of material properties. Using the 9th inversion case as an example, with the resultant aerodynamic load on the wing is employed as the evaluation metric, whose CFD simulation result is 11242.654 N. The results under different uncertainty parameters settings are summarized in Table 3 and Table 4.

The results indicate the following: (1) For all uncertainty parameters settings, the center terms of the inversed resultant aerodynamic load deviate by less than 2% from the CFD reference, demonstrating high accuracy and robustness of the inversion model. (2) As the interval radius increases linearly, the fluctuation of the resultant aerodynamic load also increases linearly, with fluctuation

Table 3
Resultant aerodynamic load results under different interval radius.

Radius	Lower boundary (N)	Upper boundary (N)	Interval center (N)	Relative error (%)	Interval radius (N)	Fluctuation level (%)
Radius 1	10891.717	11153.005	11022.361	1.959	261.288	2.371
Radius 2	10763.908	11273.265	11018.586	1.993	509.357	4.623
Radius 1	10636.954	11400.364	11018.659	1.992	763.409	6.928

levels of 2.371%, 4.623% and 6.928%, respectively. (3) For a fixed interval radius, decreasing the correlation length, namely, increasing the spatial correlation of the interval field model, leads to a gradual reduction in the fluctuation of the inversed resultant aerodynamic load.

12. An unmanned aerial vehicle (UAV) structure

This section focuses on the UAV structure depicted in Fig. 14, which features a tandem wing configuration with a larger forward wing and a smaller, similarly shaped aft wing. Given the symmetry in geometry, loading and boundary conditions, CFD and CSD simulations are conducted using a half-model to reduce computational cost. Fig. 14 (b) and (c) show the fluid and structural meshes, respectively. The wings are composed of fiber-reinforced fabric coverings filled with PMI foam. The equivalent material properties of the fabric are determined through homogenization modeling, namely, $E_{11} = E_{22} = [67.338, 70.792]$ GPa, $E_{33} = 9.893$ GPa, $G_{12} = 29.019$ GPa, $G_{12} = G_{23} = 4.159$ GPa, $\nu_{12} = 0.19$, $\nu_{13} = \nu_{23} = 0.069$ and $\rho = 2380$ kg /m^3. The material properties of PMI foam are specified as $E = 0.104$ GPa, $\mu = 0.37$ and $\rho = 30$ kg /m^3. Spanwise structural deformation of both wings is measured using 14 strain gauges, with their placement shown in Fig. 15. Wind tunnel tests are conducted across 22 cases: 8 cases at 30 m/s, 7 cases at 40 m/s and 7 cases at 50 m/s, as illustrated in Fig. 16 (a). The Reynolds numbers at different wind speeds are 1.7×10^5, 2.267×10^5 and 2.833×10^5, respectively. Additionally, aerodynamic coefficients are also recorded, which can be used to calculate the aerodynamic normal load via

$$F = \left(\frac{1}{2}\rho_F v^2\right) S_w C_L \tag{55}$$

where ρ_F is the air density; v is the wind speed; S_w is the reference wing area; and C_L is the measured normal load coefficient. To perform the ROM for aerodynamic loads, 500 samples of wind speed and angle of attack are generated, as shown in Fig. 16 (b). The dominant and mean spatial distribution features of aerodynamic loads on the forward and aft wings are displayed in Fig. 17 and Fig. 18. Results indicate that the first two principal components are sufficient to accurately characterize the high-dimensional aerodynamic loads. Below, the effectiveness of the PDNN model and the engineering application of the proposed method is explored.

12.1. The effectiveness of the PDNN model

The forward wing is selected as an example to illustrate the effectiveness of the PDNN model. The three loss functions (L_{Dat}, L_{Phy} and L_{Hyb}) introduced in Section III.B, corresponding to supervised learning, self-supervised learning, and hybrid learning strategies, are evaluated and compared. The analysis is conducted under the nominal values of uncertain structural parameters (interval center). Strain responses at measurement points under the LHS-sampled parameters are used for training responses, while the strain responses under experimental parameters are regarded as the testing responses. Both responses are derived from CSD simulations. To improve robustness against unavoidable noise interference, Gaussian noise is added to the training responses. Under such circumstances, three neural network configurations are defined: noise-free testing responses and noise-free training responses (Network 1), noisy testing responses and noise-free training responses (Network 2), noisy testing responses and noisy training responses (Network 3). Each configuration is trained under two sample conditions: a large dataset (500 samples) and a small dataset (120 samples). For the networks employing loss functions L_{Phy} and L_{Hyb}, the first three structural bending modes are selected to compute modal loads and responses within the physical-based module. The network-predicted feature coefficients are used to reconstruct modal loads, which are then compared with the reference modal loads obtained from true ROM feature coefficients. Correlation results are shown in Fig. 19 (large-sample training) and Fig. 20 (small-sample training), and the average relative error under different cases are summarized in Table 5.
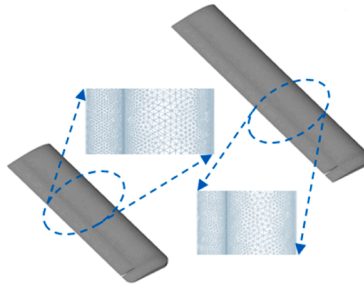
The following conclusions can be drawn: (1) When no measurement noise is considered (Network 1), all three loss functions yield highly accurate predictions, regardless of the number of training samples. The correlation coefficients between predicted and reference modal loads reach 1, with relative errors below 1%, demonstrating the strong performance of all learning strategies under ideal conditions. (2) When Gaussian noise is introduced into the testing responses, Network3 trained with noisy data consistently outperforms Network 2, which is trained without noise. As an example, under large-sample training, relative errors of all modal loads in Network 3 remain below 2%, while most in Network 2 exceed 5%. This suggests that incorporating during training may improve the network robustness to measurement disturbances. (3) For Network 3, the prediction accuracy follows the trend: self-supervised learning > hybrid learning > supervised learning. All three strategies perform well under large-sample training; while supervised learning strategy shows obvious disadvantage under small-sample training, with the relative error for the 1st order modal loads reaching 8.604%. In contrast, the self-supervised and hybrid strategies reduce this error to 0.927% and 1.225%, respectively. These

Table 4
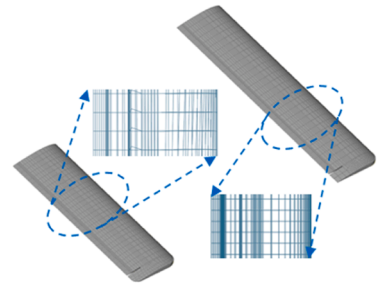Resultant aerodynamic load results under different correlation length.

Length	Lower boundary (N)	Upper boundary (N)	Interval center (N)	Relative error (%)	Interval radius (N)	Fluctuation level (%)
Length 1	10763.908	11273.265	11018.586	1.993	509.357	4.623
Length 2	10781.104	11250.929	11016.016	2.016	469.825	4.265
Length 3	10802.907	11226.404	11014.656	2.028	423.497	3.845
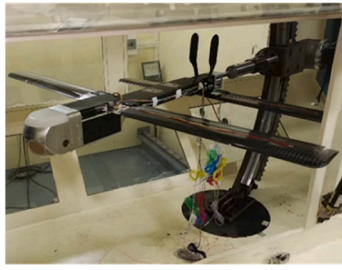
(a) The UAV structure   (b) The fluid mesh   (c) The structural mesh
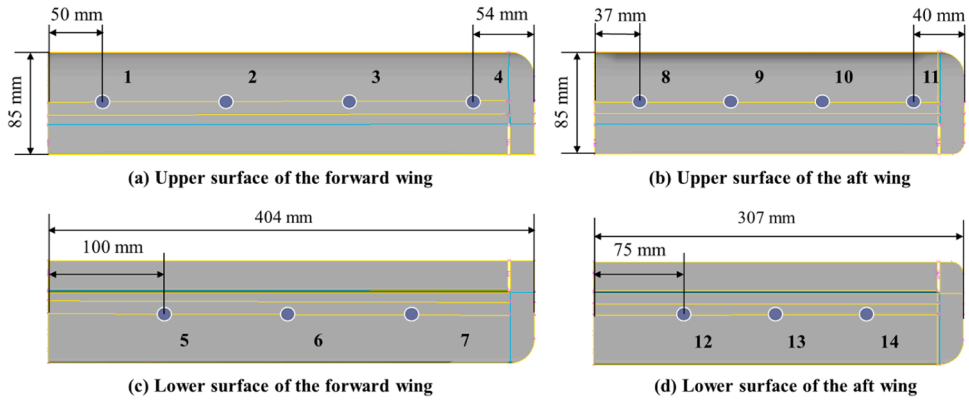
Fig 14. Schematic of the UAV structure.

(a) Upper surface of the forward wing   (b) Upper surface of the aft wing

(c) Lower surface of the forward wing   (d) Lower surface of the aft wing

Fig 15. Schematic of the UAV sensor placement.

(a) Flight parameters   (b) Parametric sampling
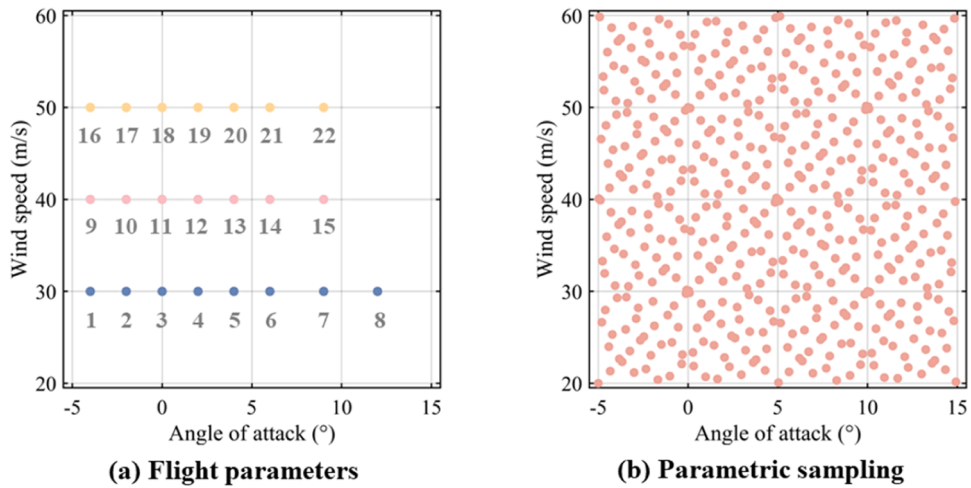
Fig 16. Parameters for experimental cases and LHS sampling.

results highlight the benefit of integrating laws into the network architecture improving the prediction accuracy and training stability, particularly under noisy or data-insufficient conditions.

12.2. Experimental validation of proposed method

To validate the aerodynamic load inversion against experimental data, uncertainty-oriented inversion is performed using the measured strain responses and the equivalent structural model Aerodynamic load distributions on the forward and aft wings are first

(a) The 1ˢᵗ order (86.893%)   **(a) The 1ˢᵗ order (99.916%)**   **(g) Mean feature**
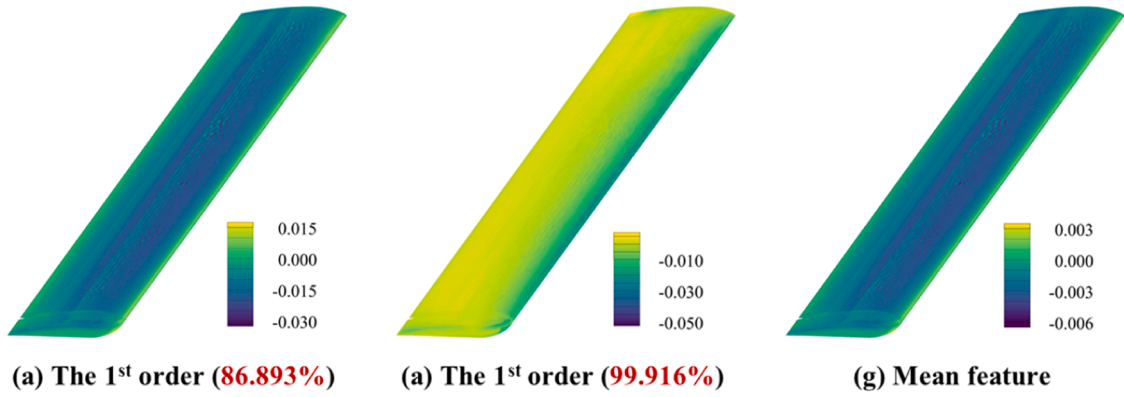
Fig 17. ROM results of aerodynamic loads on the forward wing (Units: N).

(a) The 1ˢᵗ order (95.988%)   **(a) The 1ˢᵗ order (99.951%)**   **(g) Mean feature**
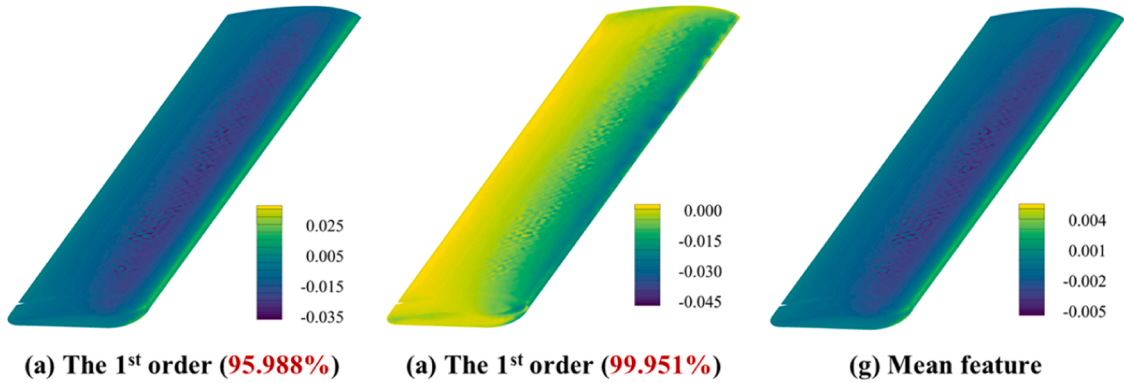
Fig 18. ROM results of aerodynamic loads on the aft wing (Units: N).

reconstructed, from which the corresponding aerodynamic normal loads are derived for comparison. It should be noted that for the 22 experimental cases, the aerodynamic normal load derived from CFD simulations exhibit certain numerical discrepancies compared to those obtained by Eq. (55) using measured normal load coefficient, but their overall trends remain consistent. To improve agreement with experimental data, the CFD-based results are calibrated accordingly. The same calibration strategy is also applied to the inversed aerodynamic normal loads. The comparison of inversed and experimental normal loads across all 22 cases are presented in Fig. 21, with statistical summaries listed in in Table 6. Furthermore, the 22nd case (the highest aerodynamic load) is selected to illustrate the spatial distribution of aerodynamic loads, as shown in Fig. 22 and Fig. 23.

The following conclusions can be drawn: (1) As shown in Fig. 21, the inversed intervals effectively envelope the experimental results, indicating the strong engineering applicability of the proposed method. Statistical analysis reveals that with increasing wind speed, both the absolute error and interval radius increase. Specifically, the mean absolute errors at 30 m/s, 40 m/s, and 50 m/s are 1.247 N, 1.302 N and 2.616 N, respectively, while the corresponding mean interval radius are 3.994 N, 6.997 N and 10.855 N. These trends are consistent with findings in Section V.A, indicating that higher wind speeds lead to more complex aerodynamic load distributions, reducing the ROM accuracy using low-order features and amplifying the impact of structural uncertainties. (2) For the 22nd case, the spatial distributions of the inversed aerodynamic loads, including lower and upper boundaries as well as the interval center, generally align with the CFD results for both wings. However, notable inversion errors appear near the leading edges, suggesting difficulties in accurately reconstructing loads in this region. Additionally, the inversed intervals exhibit greater dispersion over the upper front surfaces of the wings, reflecting increased uncertainty in those regions.

12.3. Discussion of the cost of the proposed method

In addition to accuracy, computational cost is also a crucial factor for evaluating the proposed method. In the learning stage, aerodynamic loads and responses must be computed under numerous flight parameters (Figs. 9a and 16b), which can be time-consuming but performed only once offline to capture the spatial distribution features of aerodynamic loads. This step is essential to ensure accuracy and reliability in subsequent inversion. Within the model-driven module, aerodynamic responses are projected into the modal space, leading to minimal computational demand and no extra burden on network training. In the deployment stage, once the low-order features of the aerodynamic loads are determined, the inversion task requires only a few feature coefficients within
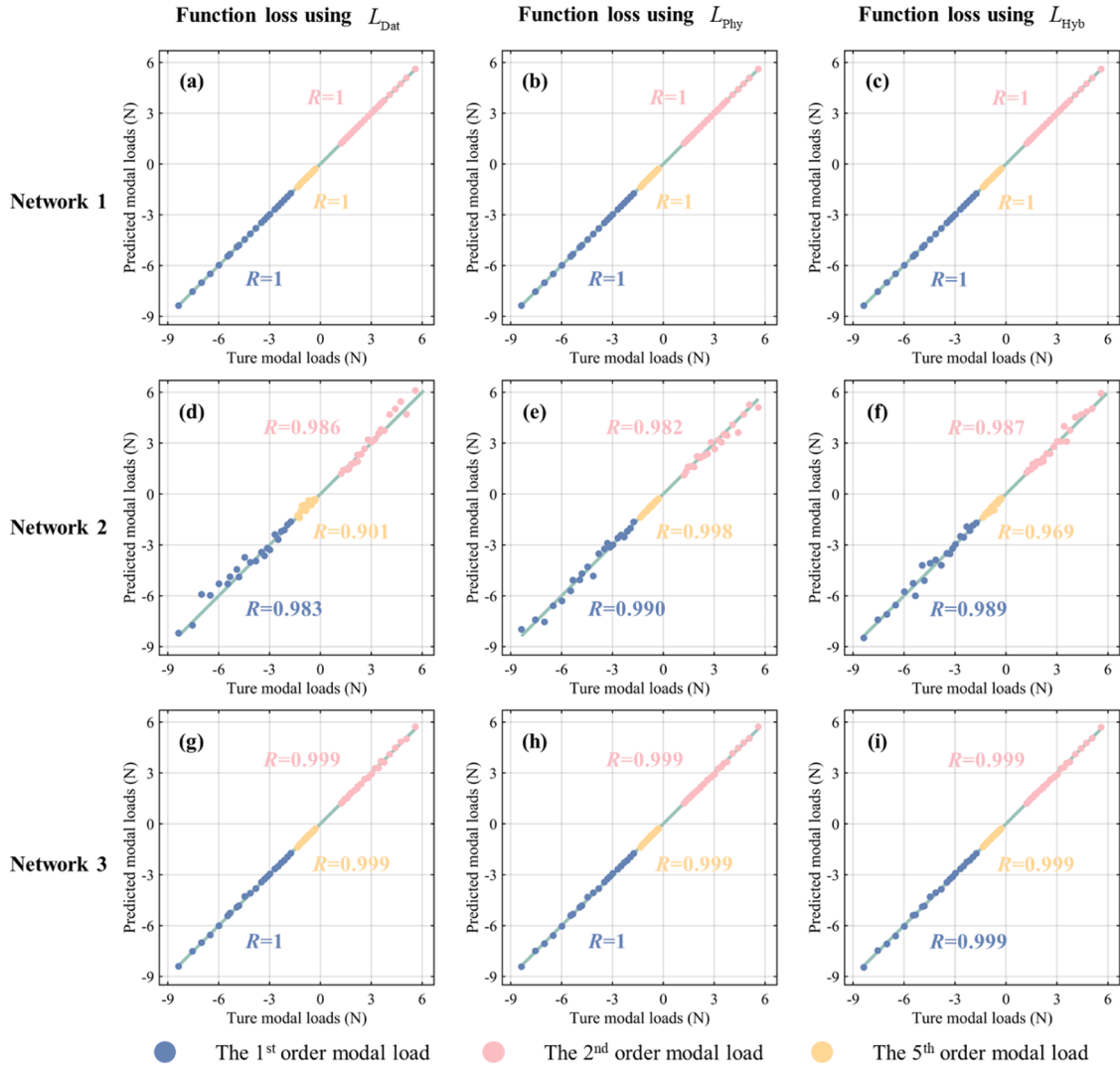
Function loss using L_{Dat} **Function loss using** L_{Phy} **Function loss using** L_{Hyb}

Fig 19. Correlation results of modal loads under large-sample training.

reduced-order subspaces rather than the full high-dimensional distributions. This significantly reduces dimensionality and makes the inversion process highly efficient. Compared with CFD simulations, the computational cost in the deployment stage decreases by several orders of magnitude, fulfilling the primary objective of ROM technique. Overall, while the learning stage entails a one-time offline investment, the deployment stage ensures practical applicability with significant computational savings.

To quantify the computational cost, the aerodynamic load inversion of the UAV structure under large-sample training is used as an illustrative example. All computations are conducted on a Lenovo Legion R9000P ARX8 laptop equipped with an AMD Ryzen 9 7945HX CPU, 64 GB DDR5 RAM, and an NVIDIA GeForce RTX 4070 GPU. For deterministic inversion at the interval center of uncertain structural parameters, the learning stage requires: 1001.783 min for CFD simulation, 2.245 min for aerodynamic load mapping, 32.025 min for CSD simulation, and 4.092 min for network training, totaling 1040.145 min. This process is dominated by the CFD simulation. In contrast, the deployment stage requires only 0.638 s to reconstruct the feature coefficients for each case. When structural uncertainties are considered, both the learning and deployment stages are repeated to construct the AKSM to estimate the interval boundaries of aerodynamic loads. In this example, the elastic moduli $E_{11} = E_{22}$ are regarded as uncertain parameters, and 9 samples are required to satisfy the convergence criterion defined in Eq. (54). This uncertainty-oriented inversion involves 1 CFD simulation and 1 aerodynamic load mapping, 9 CSD simulations, and 9 network trainings during the learning stage (totaling 1329.081 min), as well as 9 inversions during the deployment stage (totaling 5.742 s). These results demonstrate that the proposed method requires only a one-time offline cost for ROM construction and network training, while enabling highly efficient aerodynamic load inversion in practical applications.
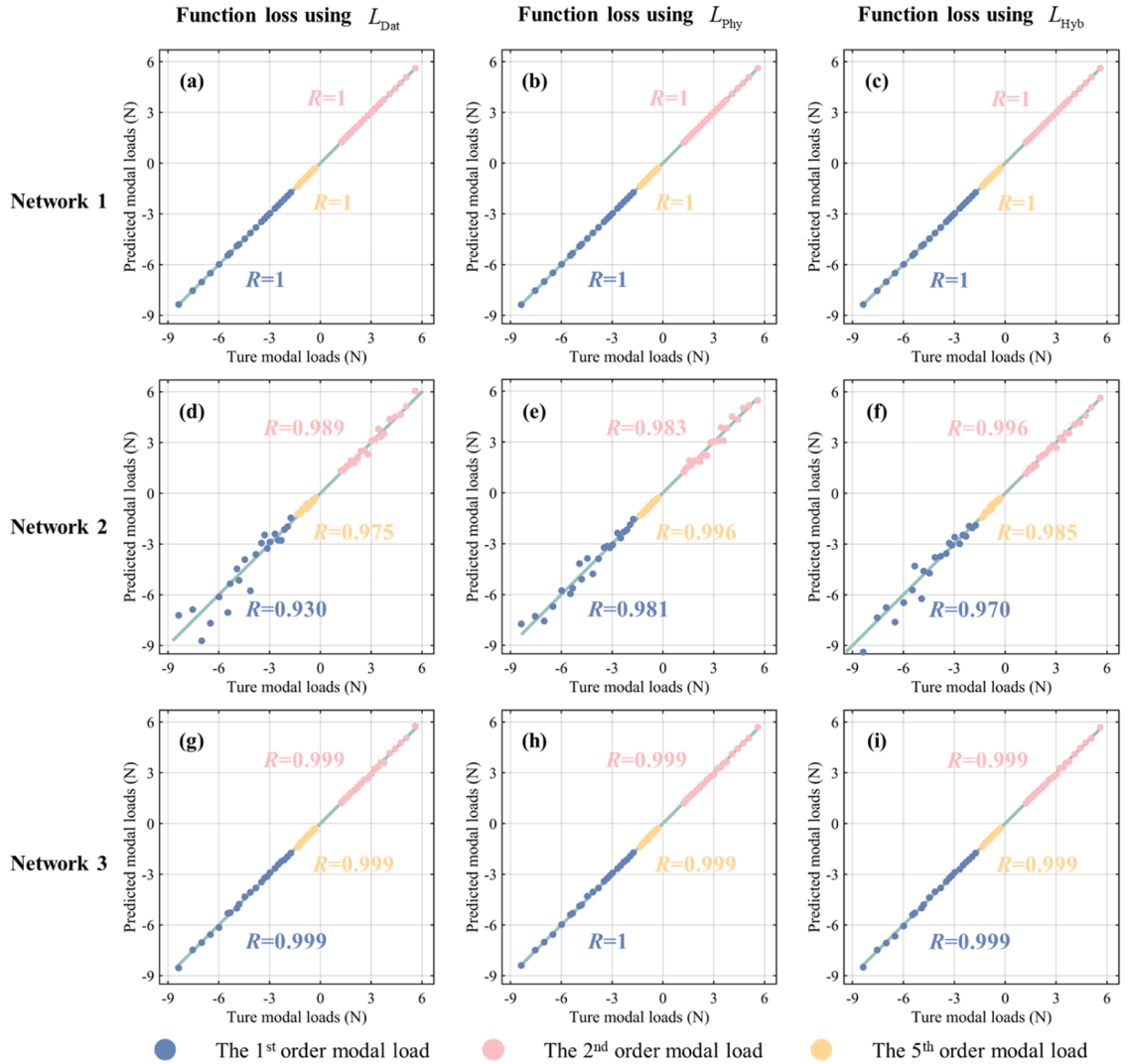
Fig 20. Correlation results of modal loads under small-sample training.

Table 5
Average relative errors of modal loads under different cases (Units: %).

Cases		L_{Dat}			L_{Phy}			L_{Hyb}		
		1st order	2nd order	3th order	1st order	2nd order	3th order	1st order	2nd order	3th order
Large-sample training	Network 1	0.178	0.173	0.954	0.120	0.155	0.855	0.107	0.127	0.910
	Network 2	6.645	6.721	12.729	5.102	6.421	2.140	5.292	5.866	9.579
	Network 3	0.826	1.903	1.503	0.923	1.350	1.345	1.179	1.333	1.422
Small-sample training	Network 1	0.208	0.131	0.898	0.155	0.208	0.809	0.125	0.136	0.867
	Network 2	12.745	5.119	7.778	6.637	6.581	3.654	8.604	3.500	5.947
	Network 3	8.604	3.500	5.947	0.927	1.217	1.445	1.225	1.420	1.477

13. Conclusion

This paper develops a hybrid physics-data-driven reduced-order modeling for aerodynamic load inversion under structural field uncertainties, which can estimate aerodynamic load boundaries from sparse response measurements. First, the ROM technique is first adopted to represent high-dimensional aerodynamic loads using spatial distribution features in low-dimensional subspaces, transforming the inversion task into a coefficient prediction problem. The PDNN model integrated data-driven and physical-based modules is then developed to predict the corresponding coefficients under the aerodynamic loads to be inversed. Eventually, the IKLD-aided
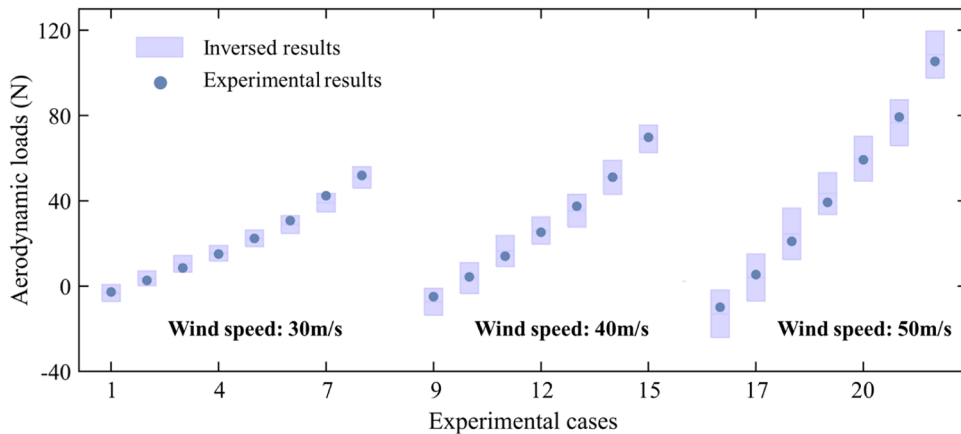
Fig 21. Comparison between inversed and experimental aerodynamic normal loads.

Table 6
Comparison between inversed and experimental aerodynamic normal loads.

Case	Experimental results (N)	CFD results (N)	Inversed interval center (N)	Absolute error (N)	Relative error (%)	Interval radius (N)	Fluctuation level (%)
1	-2.749	-3.064	-3.230	0.481	17.478	3.923	-121.457
2	2.692	3.438	3.667	0.975	36.213	3.412	93.037
3	8.510	9.805	10.474	1.964	23.083	3.814	36.412
4	15.042	16.373	15.409	0.367	2.439	3.597	23.344
5	22.360	22.738	22.439	0.079	0.355	3.821	17.030
6	30.712	29.444	28.847	1.865	6.073	4.129	14.315
7	42.390	40.053	39.087	3.303	7.793	4.294	10.986
8	51.869	52.038	50.924	0.945	1.822	4.958	9.736
9	-4.945	-7.235	-7.362	2.416	48.858	6.238	-84.742
10	4.326	3.927	3.747	0.579	13.381	7.206	192.314
11	14.024	15.288	16.414	2.390	17.043	7.233	44.066
12	25.267	26.962	26.084	0.817	3.234	6.326	24.252
13	37.452	38.222	35.367	2.085	5.567	7.602	21.493
14	51.071	50.350	50.995	0.077	0.150	7.946	15.581
15	69.758	69.438	69.007	0.751	1.076	6.425	9.311
16	-9.901	-12.635	-12.960	3.059	30.895	11.031	-85.118
17	5.387	4.885	4.047	1.339	24.865	10.982	271.338
18	20.996	22.656	24.479	3.483	16.587	12.006	49.047
19	39.282	41.079	43.364	4.081	10.390	9.806	22.613
20	59.229	58.575	59.734	0.505	0.853	10.462	17.514
21	79.256	77.832	76.611	2.645	3.337	10.734	14.012
22	105.367	107.225	108.563	3.197	3.034	10.963	10.098

interval field model is adopted to quantify structural field uncertainties, and the AKSM-based uncertainty propagation method is used to determine the boundaries of aerodynamic loads. Numerical and experimental examples validate the effectiveness of the proposed method. Results indicate that: (1) Aerodynamic loads can be effectively represented by a limited number of spatial distributions, with lower-order representations capturing more dominant aerodynamic features; (2) The PDNN exhibits strong prediction accuracy and robustness under measurement noise and small-sample training, while its self-supervised learning mechanism outperforms conventional supervised approaches in performance; (3) Structural uncertainties have a pronounced effect on aerodynamic load inversion. Accurate characterization of the spatial distribution of these field uncertainties is essential for enhancing inversion reliability.

CRediT authorship contribution statement

Yaru Liu: Writing – original draft, Software, Methodology, Conceptualization. **Lei Wang:** Writing – review & editing, Supervision, Methodology, Funding acquisition, Conceptualization. **Xuan Zhou:** Writing – review & editing, Visualization, Validation. **Zeshang Li:** Writing – review & editing, Validation, Data curation. **Yuewu Wang:** Writing – review & editing, Supervision, Funding acquisition, Data curation.
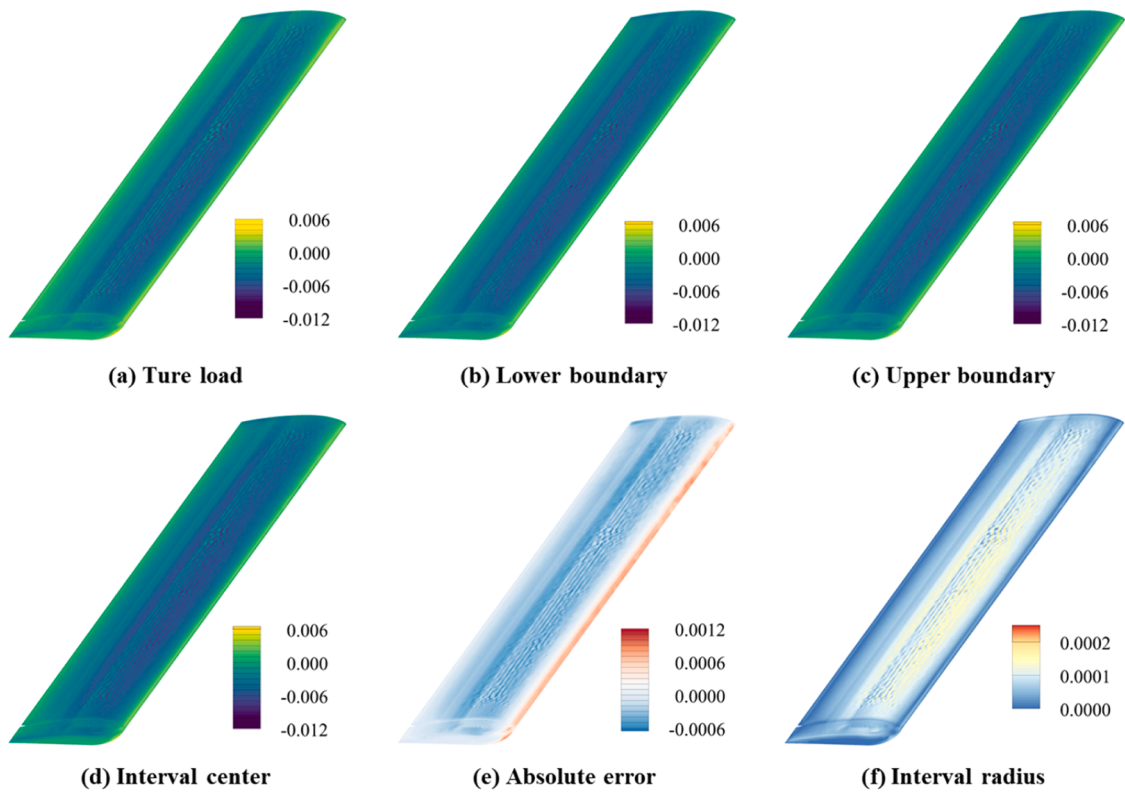
Fig 22. Inversed aerodynamic load results of the forward wing for the 22nd case (Units: N).
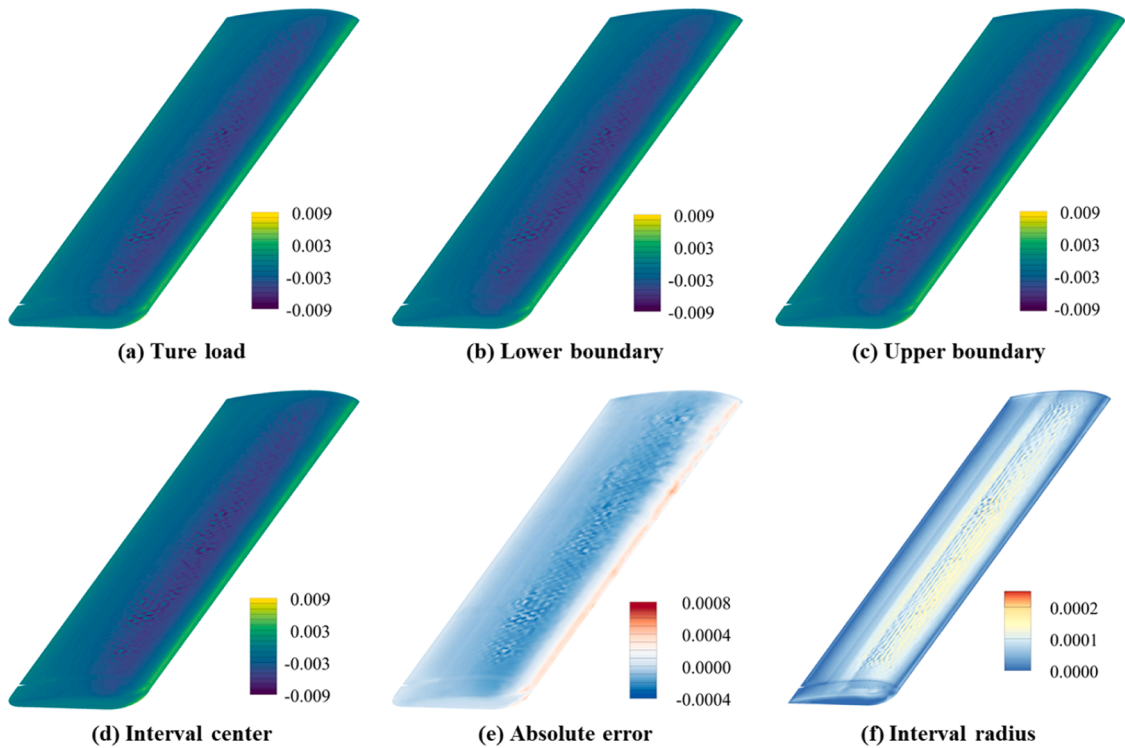

Fig 23. Inversed aerodynamic load results of the aft wing for the 22nd case (Units: N).

Declaration of competing interest

This is an original manuscript which has neither previously, nor simultaneously, in whole or in part, been submitted anywhere else.

Acknowledgment

Data availability

Data will be made available on request.

References

[1] C. Varriale, T. Lombaerts, G. Looye, Direct lift control: a review of its principles, merits, current and future implementations, Prog. Aerosp. Sci. (2025) 152.

[2] N. Mogharabin, B.I. Epureanu, A. Ghadami, Reduced order modeling and analysis of airfoil flutter using dynamics-based autoencoders, Aiaa J. (2025).

[3] R.X. Liu, E. Dobriban, Z.C. Hou, K. Qian, Dynamic load identification for mechanical systems: a review, Arch. Comput. Methods Eng. 29 (2022) 831–863.

[4] Y.X. Li, L.X. Luo, X.Y. Wang, X.Q. Zhou, L.M. Sun, Y. Xia, State-of-art review on load identification and response reconstruction to realize digital twin of infrastructures, Adv. Struct. Eng. (2025).

[5] J. Sanchez, H. Benaroya, Review of force reconstruction techniques, J. Sound Vib. 333 (2014) 2999–3018.

[6] Z.C. He, Z.M. Zhang, E. Li, Multi-source random excitation identification for stochastic structures based on matrix perturbation and modified regularization method, Mech. Syst. Signal Process. 119 (2019) 266–292.

[7] J.V. Pham, O. Ghattas, N.T. Clemens, K.E. Willcox, Real-time aerodynamic load estimation for hypersonics via strain-based inverse maps, Aiaa J. 63 (2025) 91–101.

[8] J.H. Jiang, W.X. Cui, S. Chen, X.R. Guo, J.M. Zhao, A novel dynamic load identification method based on improved basis functions and implicit newmark-β for continuous system with unknown initial conditions, Mech. Syst. Signal Process. 208 (2024) 110987.

[9] S. Gillijns, B. De Moor, Unbiased minimum-variance input and state estimation for linear discrete-time systems, Automatica 43 (2007) 111–116.

[10] S. Gillijns, B. De Moor, Unbiased minimum-variance input and state estimation for linear discrete-time systems with direct feedthrough, Automatica 43 (2007) 934–937.

[11] C.W. Coates, P. Thamburaj, Inverse method using finite strain measurements to determine flight load distribution functions, J. Aircr. 45 (2008) 366–370.

[12] Y. Zheng, S.Q. Wu, Q.G. Fei, Distributed dynamic load identification on irregular planar structures using subregion interpolation, J. Aircr. 58 (2021) 288–299.

[13] A.F. Guo, S.Q. Wu, Y. Zheng, Identify aerodynamic pressure load on a 3D wing structure from strain data using surface flattening and subregion interpolation, Aerosp. Sci. Technol. (2024) 151.

[14] T.J. Carpenter, R. Albertani, Aerodynamic load estimation from virtual strain sensors for a pliant membrane wing, Aiaa J. 53 (2015) 2069–2079.

[15] Y.R. Liu, B.F. Ng, Two-step correction and decoupled sequential framework for uncertainty-oriented dynamic force reconstruction, AIAA J., 0 1-20.

[16] H.Y. Zhang, L. Wang, Interval-updated inverse identification framework for transient coupling of loads and heat fluxes via force-thermal modal decomposition and adaptive surrogate modeling, Int. Commun. Heat Mass Transf. 166 (2025) 109223.

[17] M. Aucejo, O. De Smet, A generalized multiplicative regularization for input estimation, Mech. Syst. Signal Process. (2021) 157.

[18] M. Aucejo, O. De Smet, A novel algorithm for solving multiplicative mixed-norm regularization problems, Mech. Syst. Signal Process. (2020) 144.

[19] J.J. Liu, B.J. Qiao, Y.A. Wang, W.F. He, X.F. Chen, Group sparsity extension of "non-convex sparse regularization via convex optimization for impact force, Mech. Syst. Signal Process. (2023) 201.

[20] T.N. Tallman, L. Homa, M. Flores, J. Wertz, Damage mapping via electrical impedance tomography in complex AM shapes using mixed smoothness and bayesian regularization, Comput. Methods Appl. Mech. Eng. 414 (2023) 116185.

[21] L. Wang, L.H. Cheng, Q.H. Shi, Novel study on strain modes-based interval damage identification methodology utilizing orthogonal polynomials and collocation theories, Int. J. Numer. Methods Eng. 126 (2025) e70032.

[22] S.B. Cooper, D. DiMaio, Static load estimation using artificial neural network: application on a wing rib, Adv. Eng. Softw. 125 (2018) 113–125.

[23] D.S. Chen, F. Kaiser, J.C. Hu, D.E. Rival, K. Fukami, K. Taira, Sparse pressure-based machine learning approach for aerodynamic loads estimation during gust encounters, Aiaa J. 62 (2024) 275–290.

[24] M. Raissi, P. Perdikaris, G.E. Karniadakis, Physics-informed neural networks: a deep learning framework for solving forward and inverse problems involving nonlinear partial differential equations, J. Comput. Phys. 378 (2019) 686–707.

[25] I. Jeong, M. Cho, H. Chung, D.N. Kim, Data-driven nonparametric identification of material behavior based on physics-informed neural network with full-field data, Comput. Methods Appl. Mech. Eng. 418 (2024) 116569.

[26] J.Q. Xu, D.Q. Dai, X. Zhou, M. Giglio, C. Sbarufatti, L.T. Dong, Structural damage diagnosis and prognosis with fleet digital twin considering similarity of individual structural features, Aerosp. Sci. Technol. 168 (2026) 110983.

[27] J.X. Liu, Y.X. Li, L.M. Sun, Y.Q. Wang, L.X. Luo, Physics and data hybrid-driven interpretable deep learning for moving force identification, Eng. Struct. (2025) 329.

[28] J.M. Zhou, Y.S. Cai, L.L. Dong, B. Zhang, Z.K. Peng, Data-physics hybrid-driven deep learning method for impact force identification, Mech. Syst. Signal Process. (2024) 211.

[29] H. Zhao, C. Fu, Y.Q. Zhang, W.D. Zhu, K. Lu, E.M. Francis, Dimensional decomposition-aided metamodels for uncertainty quantification and optimization in engineering: a review, Comput. Methods Appl. Mech. Eng. 428 (2024) 117098.

[30] L. Wang, L.L. Cheng, H.Y. Xu, J.X. Hu, W.P. Chen, B. Han, Multi-source uncertainty-oriented dynamic force reconstruction framework based on adaptive fitting precise integration and optimized wavelet denoising, Struct. Multidiscip. Optim. 67 (2024) 28.

[31] X.Y. Zhao, L. Wang, Double-scale time-dependent reliable topology optimization based on the first-passage failure and interval process theories, Comput. Methods Appl. Mech. Eng. 443 (2025) 118088.

[32] J.J. Zhan, Y.J. Luo, X.P. Zhang, Z. Kang, A general assessment index for non-probabilistic reliability of structures with bounded field and parametric uncertainties, Comput. Methods Appl. Mech. Eng. 366 (2020) 113046.

[33] X. Zhou, S.X. He, L.T. Dong, S.N. Atluri, Real-time prediction of probabilistic crack growth with a helicopter component digital twin, AIAA J. 60 (2022) 2555–2567.

[34] X. Zhou, C. Sbarufatti, M. Giglio, L.T. Dong, S.N. Atluri, Copula-based collaborative multistructure damage diagnosis and prognosis for fleet maintenance digital twins, AIAA J. 61 (2023) 4735–4740.

[35] H. Ouyang, H.B. Zhou, H.Y. Wang, S.Y. Duan, X. Han, A novel sensitivity analysis method for multi-input-multi-output structures considering non-probabilistic correlations, Comput. Methods Appl. Mech. Eng. (2024) 432.

[36] Y.R. Liu, L. Wang, Multiobjective-clustering-based optimal heterogeneous sensor placement method for thermo-mechanical load identification, Int. J. Mech. Sci. (2023) 253.

[37] Y.R. Liu, L. Wang, B.F. Ng, Multitask-transfer-learning method for random-force frequency identification considering multisource uncertainties, AIAA J. (2024) 1–16.

[38] H.Y. Zhang, L. Wang, Y.R. Liu, A hybrid model-based and data-driven method for mechanical-thermal dynamic load identification considering multi-source uncertainties, Comput. Methods Appl. Mech. Eng. 435 (2025) 117662.

[39] Z.L. Guo, C.G. Zheng, B.C. Shi, Discrete lattice effects on the forcing term in the lattice Boltzmann method, Phys. Rev. E (2002) 65.

[40] G. Lenci, J.Y. Feng, E. Baglietto, A generally applicable hybrid unsteady Reynolds-averaged Navier–Stokes closure scaled by turbulent structures, Phys. Fluids 33 (2021) 105117.

[41] M. Kindelan, M. Moscoso, P. González-Rodríguez, Radial basis function interpolation in the limit of increasingly flat basis functions, J. Comput. Phys. 307 (2016) 225–242.

[42] G.B. Wright, Radial Basis Function Interpolation: Numerical And Analytical Developments, University of Colorado at Boulder, 2003.

[43] X. Zhou, L.T. Dong, M. Dziendzikowski, K. Dragan, M. Giglio, C. Sbarufatti, Real-time in-service load tracking toward airframe digital twins, AIAA J. (2025) 1–14.

[44] Z.S. Li, L. Wang, K.X. Gu, Efficient reliability-based concurrent topology optimization method under PID-driven sequential decoupling framework, Thin-Walled Struct. 203 (2024) 112117.

[45] Y.R. Liu, L. Wang, Interval sequential optimization and time-variant reliability assessment (ISOTRA) framework for dynamic stress-constrained topology design, Eng. Comput. (2025) 1–24.

[46] Z.Y. Yao, S.H. Wang, P.G. Wu, B.Y. Ni, C. Jiang, An interval finite element method based on bilevel Kriging model, Chin. J. Aeronaut. 37 (2024) 1–11.

[47] P. Glösmann, E. Kreuzer, Nonlinear system analysis with Karhunen-Loeve transform, Nonlinear Dyn. 41 (2005) 111–128.

[48] A. Sinha, V. Shaikh, Solving bilevel optimization problems using kriging approximations, IEEE Trans. Cybern. 52 (2021) 10639–10654.

[49] D.W. Zhan, H.L. Xing, Expected improvement for expensive optimization: a review, J. Glob. Optim. 78 (2020) 507–544.